

High- T_C Superconductivity in Hydrogen Clathrates Mediated by Coulomb Interactions Between Hydrogen and Central-Atom Electrons

Dale R. Harshman¹ · Anthony T. Fiory²

27 May 2020[†]

Abstract

The uniquely characteristic macrostructures of binary hydrogen-clathrate compounds MH_n formed at high pressure, a cage of hydrogens surrounding a central-atom host, is theoretically predicted in various studies to include structurally stable phonon-mediated superconductors. High superconductive transition temperatures T_C have thus far been measured for syntheses with $M = \text{La, Y, and Th}$. In compressed LaH_{10} , independent studies report T_C of 250 K and over 260 K, a maximum in T_C with pressure P , and normal-state resistance scaling with temperature (suggesting unconventional pairing). According to reported band structure calculations of $Fm\bar{3}m$ -phase LaH_{10} , the La is anionic, with the chemical valence electrons appearing evenly split between La and H_{10} . Thus, compressed LaH_{10} contains the combination of structure, charge separation and optimal balanced allocation of valence electrons for supporting unconventional high- T_C superconductivity mediated by Coulomb interactions between electronic charges associated with La and H_{10} . A general expression for the optimal superconducting transition temperature for MH_n clathrates is derived as $T_{C0} = k_B^{-1} \Lambda [(n + \nu)/2A]^{1/2} e^2/\zeta$, where Λ is a universal constant, $(n + \nu)$ is the chemical valence sum per formula unit, taking unity for H and ν for atom M , A is the surface area of the H-polyhedron cage, and ζ is the mean distance between the M site and the centroids of the polyhedron faces. Applied to $Fm\bar{3}m$ LaH_{10} , T_{C0} values of 249.8(1.3) K and 260.7(2.0) K are found for the two experiments. Associated attributes of charge allocation, structure, effective Coulomb potential, and H-D isotope effect in T_C of $Fm\bar{3}m$ LaH_{10} and $Im\bar{3}m$ H_3S are discussed, along with a generalized prospective for Coulomb-mediated superconductivity in MH_n .

Keywords LaH_{10} · Superhydrides · Superconductivity · T_C · Coulomb mediation

Dale R. Harshman
drh@physikon.net

¹ Department of Physics, The College of William and Mary, Williamsburg, VA 23187, USA

² Department of Physics, New Jersey Institute of Technology, Newark, NJ 07102, USA

[†] Harshman D. R. and Fiory A. T., J. Supercond. Nov. Magn. (2019)
<http://dx.doi.org/10.1007/s10948-020-05557-4>
public share: <https://rdcu.be/b411V>

1 Introduction

Binary hydride clathrates MH_n are a class of compounds comprising a central atom surrounded by a polyhedron hydrogen cage and have been designated as superhydrides. Following earlier theoretical results [1], superconductivity at high temperatures has been predicted in dozens of such (and other) hydride compounds under compression, assuming strong-coupled electron-phonon theory [2-4]. Notably, the superconductors LaH_{10} [5, 6], YH_n ($n = 4, 6, 9$) [5-9], and ThH_n ($n = 9, 10$) [6, 10] have been experimentally verified in [11-13], [14, 15], and [16], respectively. The LaH_{10} clathrate, exhibiting superconductivity at temperatures of about 250 K [12] and above 260 K [13] for applied pressures $P \sim 137 - 218$ GPa, currently holds the record for the highest transition temperature, T_C . Electron-phonon interaction theory rooted in strong-coupling Migdal-Éliashberg methodology [17-19], density functional theory, or *ab initio* methods [4, 20], predicts T_C for LaH_{10} spanning a broad range of 199 – 288 K [4-6, 21-26] and monotonically decreasing with increasing pressure [5, 24-26]. The $Fm\bar{3}m$ phase of LaH_{10} is theoretically stable at $P = 129 - 264$ GPa [25].

Although electrical resistance measurements are generally employed as the principal indicator of superconductivity, the reported data already indicate unconventional behavior, particularly for LaH_{10} and YH_9 . For each compound, a maximum T_C is observed in its pressure dependence, referred to as a “dome” in T_C -vs.- P [12, 14], setting bounds on pressure for maximum T_C as found in unconventional high- T_C superconductors, such as in the compressed phases of Cs_3C_{60} [27]. Differences between the LaH_{10} samples reported in [12] and [13] indicate a 10-K increase in T_C related to increased pressure, similar to the influence of higher synthesis pressure noted in [28] and the pressure

dependence reported in [29]. Negative pressure shifts in T_C calculated in [5, 23-26] evidently do not capture these experimental findings. In the normal state, the electrical resistance of LaH_{10} and YH_9 samples is found to be nearly proportional to temperature [12-14, 30], exhibiting the characteristic absence of resistance saturation of unconventional high- T_C superconductors [31].

A review of conventional electron-phonon coupling theory in [4] includes a listing of numerous computational flaws that remain to be addressed.¹ As independent corroboration of phonon mediation has yet to be convincingly established [36], alternative considerations of electronic mechanisms are being developed, particularly in view of the high pressures [37], correspondences to high- T_C cuprates [38] and limitations on the Fermi temperatures [39].

An unconventional Coulomb-mediated high- T_C mechanism, wherein superconductivity originates locally within the metal-clathrate structure, is proposed herein which is independent of conventional phononic pairing involving the extended crystalline lattice. The proposed model is a novel adaptation of the inter-reservoir Coulomb-mediated superconducting pairing theory, first introduced in [40], and successfully applied to compressed $Im\bar{3}m$ H_3S [41],² which asserts that quasiparticle pairing arises from Coulomb interactions between charges in two adjacent, spatially-separated reservoirs, designated as type I and type II. In

¹ The layered FeH_5 , synthesized with no demonstration of superconductivity [32], is predicted to be superconducting in [33, 34] and non-superconducting in [35].

² Note that here is a typographical error at the end of Section 3 (p. 5) of [41] which should read, “ $\ell = (A/\sigma)^{1/2} = 2.883 \text{ \AA}$,” with the reported T_{C0} remaining unchanged.

the case of compressed LaH_{10} , the hydrogen polyhedron cage is identified as type I (superconducting) and the central La as type II (mediating). These charge reservoirs are separated by an interaction distance ζ determined as the mean distance between the polyhedron center and the centroids of its faces. The requisite balance between type I and type II charges for optimal high- T_C superconductivity posited in [40] appears satisfied by the anionic nature of the La charge as revealed by theoretical band structure of LaH_{10} at high pressure [5, 22]. As shown in Section 2, each reservoir contains a number of charges per formula unit σ equal to one-half of the total number of chemical valence charges, which is optimally 13 for LaH_{10} .

In Section 2, a general expression for T_{C0} is derived for $M\text{H}_n$ clathrates and applied to calculate T_{C0} of LaH_{10} . Section 2 also considers the question of superconductivity and charge equilibrium between the two reservoirs in LaH_{10} , YH_n , and ThH_n , expressing T_{C0} as a function of the average H-H bond length in the binary clathrates. Section 3 considers potential superconducting clathrates in terms of inter-reservoir charge equilibrium and phase purity. Also, data for the isotope effect in T_C reported in [12] are analyzed from the perspective of sample-quality variations, similar to that done for $Im\bar{3}m$ H_3S [42]. Finally, implications of the Coulomb potential signature in optical reflectivity data and relevant electron-phonon coupling in LaH_{10} , are considered. Results are summarized and conclusions drawn in Section 4. The Appendix contains theoretical and experimental T_C -vs- P results for LaH_{10} , YH_9 , and YH_6 (Section A1), normal-state resistance (Section A2), pressure dependence of the LaH_{10} lattice parameter (Section A3), and accuracy and systematic errors of the interlayer Coulombic pairing model (Section A4).

2 Coulomb-Mediated Superconductivity in $M\text{H}_n$

Experimental bases for unconventional high- T_C superconductivity and optimal T_C are the non-monotonic “dome”-shaped pressure dependence in T_C reported for $Fm\bar{3}m$ LaH_{10} [12] and $P6_3/mmc$ YH_9 [14]. This signature feature of high- T_C materials defines optimal P and T_C at the top of the dome where T_C is highest [31]. As shown by the samples numbered 1–6 in [12], T_C systematically increases with increasing P at sub-optimal pressures. Conventional electron-phonon interaction theory predicts a fundamentally different monotonic decrease in T_C with increasing pressure above a structural stability threshold [24-26], and resembling the behavior of depressed T_C at pressures above optimal [12, 13]. Values of optimal T_C and corresponding pressures are determined from data for LaH_{10} [12, 13] and YH_9 [14] (Section A1).

Unconventional high- T_C superconductivity in the hydrogen clathrates is further demonstrated in the temperature dependence of the normal-state resistance, $R_N(T)$. As is discussed in Section A2, $R_N(T)$ for both $Fm\bar{3}m$ LaH_{10} [12, 13] and $P6_3/mmc$ YH_9 [14] is linear, exhibiting an absence of saturation at high temperature, indicative of an absence of strong electron-phonon coupling, and a near-zero intercept extrapolation to zero temperature, $R_N(T \rightarrow 0) \sim 0$. Given that both materials exhibit this unconventional behavior, it is unlikely coincidental. Recall that the lack of saturation and $R_N(T) \propto T$ are well-recognized features of optimal high- T_C materials [31, 43], strongly suggesting a pairing mechanism akin to that of other (unconventional) high- T_C superconductors. In optimally- and over-doped high- T_C cuprates, $R_N(T) \propto T$ is generally attributable to “Planckian” dissipation [44, 45]. Analysis of R_N in Section A2 indicates Planckian

dissipation in LaH_{10} comparable to the high- T_C cuprates [46-48].

Superconductive pairing in high- T_C superconductors is successfully modeled by Coulomb interactions between charges in spatially separated charge reservoirs [40, 41, 49-55]. Developed initially to describe indirect Coulombic pairing interactions between charges in adjacent extended layers, this unique theory is also applicable to extended three-dimensional (3D) lattices, such as the compressed phases of Cs_3C_{60} [49] and H_3S [41], in which charges are similarly separated into two reservoirs. To date, this approach has been validated with statistical accuracy of ± 1.30 K (or $\pm 4\%$) in T_{C0} for 53 different materials from ten disparate superconducting families; the aforementioned 3D compounds [41, 49], layered cuprates, ruthenates, rutheno-cuprates, iron pnictides, BEDT-based [bis(ethylenedithio)tetrathiafulvalene] organics [40, 50, 51], iron chalcogenides [52], intercalated group-4-metal nitride halides [53, 54] and gated twisted bilayer graphene [55], with measured T_{C0} values ranging from ~ 2 to 200 K. Optimization resulting in a maximum transition temperature is typically accomplished via doping and/or pressure-induced charge transfer.

In general terms, the type I reservoir is identified with the dominant superconducting condensate while the type II reservoir is associated with mediating charges. However, in some instances, both reservoirs serve dual superconducting and mediating purposes [41, 53]. Given the electronic and structural features required as described, the model predicts an optimal transition temperature T_{C0} of a homogeneous high- T_C superconductor given by the algebraic formula scaling with the potential energy e^2/ζ [40],

$$T_{C0} = k_B^{-1} (\Lambda/\ell) e^2/\zeta, \quad (1)$$

where ζ is the perpendicular distance between the two interacting charge reservoirs, and the length $\ell = (\sigma\eta/A)^{-1/2}$ is the linear interaction charge spacing defined by the participating charge σ (a dimensionless fraction) per unit area A of the type I reservoir. The factor η is the number of type II mediating layers in certain topographies with multiple layers and equals unity for the binary superhydride clathrates. The constant $\Lambda = 0.007465(22) \text{ \AA} = 1.933(6)\lambda_C$ is previously determined experimentally to a $\pm 0.3\%$ accuracy in [40, 41] and expressed in terms of the reduced Compton wavelength λ_C . The microscopic description leading to Eq. (1) is discussed in [41].

For the superhydride clathrates $M\text{H}_n$, the type I charge reservoir structure is identified as the cage of hydrogen ions, each located at the vertices of a polyhedron, and the type II charge reservoir is the enclosed central metal ion M . The polyhedron is treated as a closed layer that is folded upon itself in 3D, and thus its surface area determines A for the type I reservoir. The average of the distances ζ_i between the polyhedron center and its polygon-face centers, weighted by their areas A_i , determines ζ according to

$$\zeta = \sum_i \zeta_i A_i / A. \quad (2)$$

These definitions of A and ζ are drawn from earlier work on Cs_3C_{60} , following methods initially established in [40] for extended layered structures. The hydrogen cage provides the same type I function as the C_{60} in compressed Cs_3C_{60} , wherein the corresponding type II reservoir comprises nearest-neighbor cesium ions located outside of the C_{60} structure [49].

The total charge per formula unit forming the superconductive condensate [40] is created

for some materials by doping through atomic substitutions in one or both charge reservoirs [52] while it is inbuilt in others by available chemical valence electrons. An example of the latter is the three valence electrons from Cs per formula unit of Cs_3C_{60} [49]. Here, the participating charge σ is determined by multiplying the total number of electron charges by the inter-reservoir sharing factor γ , which follows the charge allocation rules in [40] (see also [51]). For the MH_n clathrates only rule (1b) applies,³ specifying $\gamma = 1/2$ for equal sharing of the total charge between the two reservoirs. The total charge number equals the sum of the full chemical valence per formula unit of M with valence ν and the n hydrogens, each with unity valence. Whether the charge $(n + \nu)$ is equally shared between M and H_n ions, as is found for H_3S [41], remains to be determined by examining the particular electronic structure of each MH_n compound. For optimal charge allocation between the two reservoirs, $\gamma = 1/2$ and the resulting equation for the participating charge

$$\sigma = (n + \nu)/2, \quad (3)$$

thus determines the length ℓ in Eq. (1),

$$\ell = [(n + \nu)/2A]^{-1/2}, \quad (4)$$

which then becomes

$$T_{\text{C}0} = k_{\text{B}}^{-1} \Lambda [(n + \nu)/2A]^{1/2} e^2 / \zeta. \quad (5)$$

Optimization in T_{C} is achieved via hydrostatic compression, suggesting a charge transfer process which induces equilibrium between the two charge reservoirs. Making correspondence to the prescription of rule (1b) [40], the M ion (type II) acquires (relative to the

neutral atom) the optimal number $(\sigma - \nu) = (n - \nu)/2$ of electrons and the n H ions (comprising type I) collectively give up the number $(n - \sigma) = (n - \nu)/2$ of electrons, equivalent to forming holes of like number.

The concept of charge equilibrium between the interacting structures of the two reservoirs is an important requirement for achieving an optimal high- T_{C} superconductive state within the interlayer Coulomb mediation model. It specifies equality of reservoir charges σ in 3D structures such as Cs_3C_{60} [49] and the binary clathrates MH_n , which is equivalent to equal areal charge densities ℓ^{-2} for interacting layers in 2D layered reservoir structures as derived in [40]. One thus expects adherence to charge equality for optimal high- T_{C} superconductivity in the binary superhydrides. Charge equilibrium between the two reservoirs, which is not explicitly considered in electron-phonon theory, dictates both the presence and quality of the superconductivity in MH_n clathrates. In contrast, superconducting behavior in electron-phonon theory is determined by the dense hydrogen-clathrate sublattice [26] and the mass [6], rather than the chemical details [8] of the enclosed atom. In the following, structure, charge allocation, and optimal $T_{\text{C}0}$ are determined for LaH_{10} (Section 2.1), MH_n generally (Section 2.2), and other clathrates such as YH_n (Section 2.3).

2.1 LaH_{10} – Calculation of $T_{\text{C}0}$

From Eq. (3), the participating charge fraction $\sigma = (10 + 3)/2 = 6.5$ is obtained by adding up the valence electrons in the atoms constituting a formula unit of LaH_{10} , counting $n = 10$ for the ten H $1s^1$ and $\nu = 3$ for a single La $5d^1 6s^2$. Although 6.5 exceeds the normal number of 3 valence electrons in atomic La, band structure calculations of $Fm\bar{3}m$ LaH_{10} at $P = 300$ GPa show formation of hybridized La- f and H- s

³ Rule (1b) from [40] (see also [51]) reads that “The doping is shared equally between the hole and electron reservoirs, resulting in a factor of 1/2.”

orbitals, rendering an anionic character to the La [22]. An electron density contour map presented in Fig. 1(b) of [22] also shows that the La anion is separated from its neighboring hydrogen ions by a shell of comparatively reduced electron density of approximately $0.5 - 0.6 \text{ \AA}^{-3}$. By defining boundaries between ions along such minima in local electron density, one estimates that about $46 \pm 4\%$ of the total valence electronic charge is on the anionic La, with $44 \pm 4\%$ at the eight H1 ions (also designated anionic in [22]) and $10 \pm 1\%$ at the two H2 ions (designated cationic in [22]); the total number of electrons estimated in this manner is $14 \pm 1 \approx (n + \nu)$ per formula unit. Hence, this analysis of results from band structure calculations suggests that the total valence charge is nearly equally divided between the La and the ten H ions, affirming application of Eq. (3) and its derivation from rule (1b) [40].

The anionic character of La is also indicated by the partial density of electron states (PDOS) for LaH_{10} at 250 GPa in occupied s , p , d , and f orbitals projected onto La, as shown in Fig. S3(b) of [5]. The electron charge on H_{10} is determined by integrating the PDOS shown for orbitals projected onto H. Over the plotted range $-1.5 \text{ Ry} \leq E \leq E_{\text{F}}$, the H-projected s and p orbitals contain charges $5.7e$ and $0.7e$, respectively, giving a total of at least $6.4e$ on H_{10} . Integrated La-projected PDOS is at least $15.5e$ and evidently includes semi-core states. Unplotted PDOS for $E < -1.5 \text{ Ry}$ might slightly increase these numbers. The number of electron charges in the type I H_{10} reservoir at 250 GPa is evidently within 1.5% from being equal to the number $\sigma = 6.5$ per formula unit determined from rule (1b) and calculated according to Eq. (3).

In the $Fm\bar{3}m$ structure of LaH_{10} the type I polyhedron cage comprises 32 hydrogens at

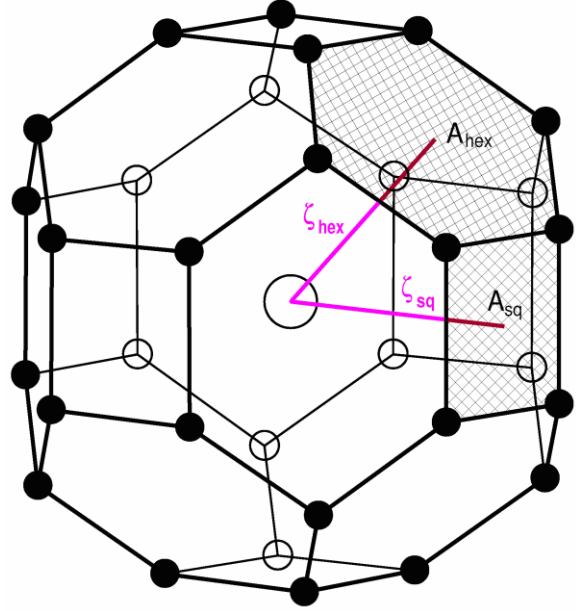


Fig. 1 The LaH_{10} clathrate structure, with hydrogens (small spheres) at the vertices of a chamfered cube polyhedron and La (large sphere) at center. The two interaction lengths, ζ_{hex} and ζ_{sq} extend from the center to the centroids of the hexagonal and square polyhedron faces of area A_{hex} and A_{sq} , respectively

the vertices of a chamfered cube with square and irregular hexagon faces (see Fig. 1). The 24 type H1 ions at vertices of adjoining square and hexagon faces are shared among 3 polyhedra and the 8 type H2 ions at vertices of adjoining hexagon faces are shared among 4 polyhedra, allocating $24/3 = 8$ H1 ions and $8/4 = 2$ H2 ions, respectively, per formula unit. Structure theory has determined irregular chamfered cube geometry with H1-H1 bonds longer than H1-H2 bonds [5, 22].

Recognizing that the hydrogen ion sites and occupancies have not been directly determined from x-ray diffraction of $Fm\bar{3}m$ LaH_{10} , the quantities in Eq. (2) are calculated using theoretical hydrogen bond lengths in irregular chamfered cube structures [5, 22], in combination with measurements of the lattice parameter a [12, 13]. Defining the ratio of the H1-H1 to H1-H2 bond lengths as $r = d_{\text{H1-H1}}$

$d_{\text{H1-H2}}$ and the associated anisotropy factor $f = (r - 1)/(r + 1)$, the average H-H bond length, expressed in terms of lattice parameter, is $d = a [2 + 4/3^{1/2} + f(2 - 4/3^{1/2})]^{-1}$. In the irregular chamfered cube polyhedron, four H1-H1 bonds form 6 square faces of area $A_{\text{sq}} = (rd)^2$, two H1-H1 and four H1-H2 bonds form 12 irregular hexagon faces of area $A_{\text{hex}} = [8 \cdot 2^{1/2}(1/3 + r/3^{1/2})/(1 + r)]d^2$, and the total area of the polyhedron is thus $A = 6A_{\text{sq}} + 12A_{\text{hex}}$. Distances measured from polyhedron center are $\zeta_{\text{sq}} = d [(r + 4/3^{1/2})/(1 + r)]$ to the square face centers and $\zeta_{\text{hex}} = d [2^{-1/2}(r + 2/3^{1/2})/(1 + r)]$ to the hexagon face centers; the average distance weighted by face areas gives $\zeta = (6A_{\text{sq}}\zeta_{\text{sq}} + 12A_{\text{hex}}\zeta_{\text{hex}})/A$. These distance and area parameters are illustrated in Fig. 1. Below, the expressions for d , A , and ζ are evaluated for $r = 1.077$, which is obtained by averaging the theoretical pressure dependence of $d_{\text{H1-H1}}$ and $d_{\text{H1-H2}}$ calculated in [5] over the optimal range $P = 169 - 192$ GPa determined from experiment (Section A1).

Data presented in the inset of Fig. 1 of [12] for $Fm\bar{3}m$ LaH_{10} show the highest superconducting transition temperature occurring for sample 5 at $T_C = 251(1)$ K at a

corresponding average pressure $P = 169(4)$ GPa (Section A1). The corresponding lattice parameter $a = 5.009(14)$ Å is determined by the variation of a -vs.- P derived from the experimental data (Section A3). The formulae given above then evaluate to $d = 1.165(3)$ Å, $A = 50.29(27)$ Å², $\zeta = 1.795(5)$ Å, $\ell = 2.781(8)$ Å, and $T_{C0} = 249.8(1.3)$ K. These results are listed in the first data row of Table 1.

A complete superconducting resistance transition is shown in Fig. 1 of [13] for a sample at initial pressure of 188 GPa, where the authors observe an appreciable drop in resistance at 260 K upon cooling (blue cooling curve) and a pressure of 196 GPa after warming back to 300 K. As discussed in Section A1, the superconducting onset $T_C = 262(1)$ K is considered to be optimal at the average pressure of $P = 192(4)$ GPa. The corresponding lattice parameter is $a = 4.903(18)$ Å. One thereby obtains for this sample the values $d = 1.141(4)$ Å, $A = 48.18(36)$ Å², $\zeta = 1.757(7)$ Å, $\ell = 2.723(10)$ Å, and calculated $T_{C0} = 260.7(2.0)$ K, which are included the second data row of Table 1.

Third row entries in Table 1 describe results for compressed $Im\bar{3}m$ H_3S . The

Table 1 Experimental transition temperatures T_C at applied pressures P are given for $Fm\bar{3}m$ LaH_{10} from data in [12, 13] and for $Im\bar{3}m$ H_3S from data in [56]. Lattice parameter a is determined by P . Theoretical parameters listed are the participating charge σ , average H-H bond length d , surface area A (H_{32} polyhedron for $Fm\bar{3}m$ LaH_{10} , cubic faces for $Im\bar{3}m$ H_3S [41]), interaction distance ζ , mean spacing between participating charges ℓ and calculated optimal transition temperature T_{C0} , as defined in the text

Expt. Ref.	T_C (K)	P (GPa)	a (Å)	σ	d (Å)	A (Å ²)	ζ (Å)	ℓ (Å)	T_{C0} (K)
LaH_{10} ($Fm\bar{3}m$)									
[12]	251(1)	169(4)	5.009(14)	6.5	1.165(3)	50.29(27)	1.795(5)	2.781(8)	249.8(1.3)
[13]	262(1)	192(4)	4.903(18)	6.5	1.141(4)	48.18(36)	1.757(7)	2.723(10)	260.7(2.0)

H_3S ($Im\bar{3}m$)									
[56]	201	155	3.082(5)	3.5	2.180(4) ^a	28.50(9)	2.180(4)	2.854(5)	200.6(3)

^a d is intra-sublattice H-H distance

measurement of T_C is taken from the most recently available data, identified as “155 GPa: 11/2018” in Fig. 1 of [56], exhibiting a significantly sharper transition than that reported previously [57]. In [41] showing Coulomb-mediated superconductive pairing in H_3S , a charge of $\sigma = 3.43 \pm 0.10$ is derived from the average of integrated PDOS for H s electrons calculated in [58] and [59] (per H_3 unit). Much of the PDOS for the sulfur s orbital lies deep in energy, diminishing near E_F , as shown in Fig. 2b of [58] and in Fig. 2 of [60]. Evidently, the two $3s^2$ electrons from atomic S fill localized core-like orbitals such that the available valence electrons are dominated by the four $3p^4$ electrons of the S atom and the three $1s$ electrons from H_3 . In reference to the value of σ derived from projected H s orbitals, inter-reservoir charge equilibrium is evidently established with S valence $\nu = (3.86 \pm 0.20) \approx 4$ and $n = 3$ in Eq. (3) and produced by transfer of $(0.47 \pm 0.10)e \approx e/2$ valence electron charge from S to H_3 . Model parameters determined previously [41] are shown for comparison, but in this case using Eq. (3) with $n = 3$ and $\nu = 4$ to give $\sigma = 7/2 = 3.5$ and $T_{C0} = 200.6(3)$ K.

Figure 2 shows the experimental values of T_C vs. $(\ell\zeta)^{-1}$ from the preceding calculations for $Fm\bar{3}m$ LaH_{10} and given in Table 1. Horizontal error bars correspond to uncertainties in pressure; uncertainties in T_C , smaller than symbols sizes, are not shown. For comparison, the corresponding result for H_3S [56] from Table 1 is shown by the triangle symbol. The solid line in Fig. 2 represents theoretical dependence of T_{C0} on $(\ell\zeta)^{-1}$ defined by Eq. (1). Given the essential differences in structure and bonding between $Fm\bar{3}m$ LaH_{10} and $Im\bar{3}m$ H_3S (noted in [61]), it is remarkable that theory derived from the interlayer Coulomb-mediation pairing model accurately determines T_{C0} for both hydride families. A comparison of the two optimal

LaH_{10} clathrate samples with H_3S and optimal materials from other unconventional high- T_C families is given in Section A4.

2.2 Optimal MH_n Clathrates

With the proviso that the optimization criterion could be satisfied for some binary MH_n clathrates other than LaH_{10} , it is useful to note that Eqs. (2) – (5) have a general functional dependence on the participating charge σ and average H-H bond length d in the form

$$T_{C0} = C_n \sigma^{1/2} k_B^{-1} \Lambda e^2 / d^2, \quad (6)$$

where $C_n = A^{-1/2} \zeta^{-1} d^2$ depends only on the H-cage structure (cubic symmetries have $d \propto a$ and $T_{C0} \propto a^{-2}$). Values of A/d^2 , ζ/d , and C_n are given in Table 2 for exemplary $Fm\bar{3}m$ YH_3 , $Im\bar{3}m$ YH_6 , $P6_3/mmc$ YH_9 and $Fm\bar{3}m$ YH_{10} clathrates corresponding to $n = 3, 6, 9$ and 10 [6, 8]. The corresponding theoretical crystal symmetries are H-cage polyhedral structures, $[4^{12}]$ (rhombic dodecahedron), $[4^6 6^8]$ (truncated octahedron), $[4^6 5^6 6^6]$ (irregular polygon faces) and $[4^6 6^{12}]$ (irregular

Table 2 Geometric factors for hydrogen-cage polyhedra in MH_n with specified structures. Polyhedron surface area A and average distance ζ between the polyhedron center and its face-polygon centroids, weighted by area, are given normalized to average polyhedron edge length d , which determine the numerical coefficient $C_n = A^{-1/2} \zeta^{-1} d^2$ in Eq. (6)

n	Structure	Vertex number	A/d^2	ζ/d	C_n
3	$[4^{12}]^a$	14	11.314	0.8165	0.3641
6	$[4^6 6^8]^b$	24	26.785	1.2672	0.1525
9	$[4^6 5^6 6^6]^c$	29	31.167	1.4214	0.1260
10	$[4^6 6^{12}]^d$	32	37.025	1.5402	0.1067

^a Rhombic dodecahedron

^b Truncated octahedron

^c $P6_3/mmc$ YH_9 [6]

^d Irregular chamfered cube, assumed edge asymmetry ratio $r = 1.08$ [5, 8]

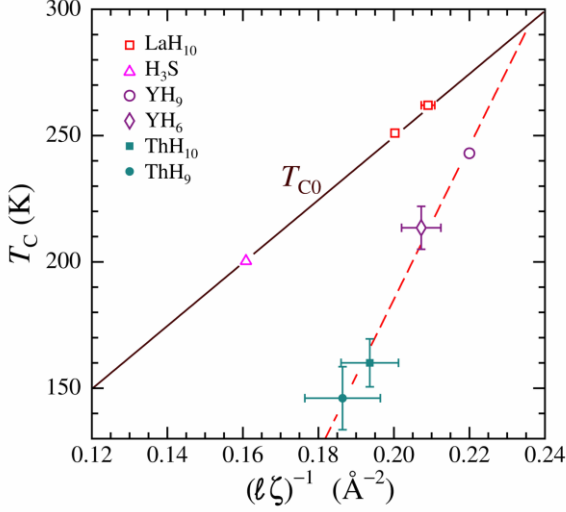


Fig. 2 Measured transition temperatures T_C for $Fm\bar{3}m$ LaH_{10} [12, 13] and $Im\bar{3}m$ H_3S [56] are plotted against $(\ell\zeta)^{-1}$, as determined from the data in Table 1. The solid line represents the interlayer Coulomb pairing theory for T_{C0} defined in Eq. (1). Results for the mixed-phase, non-optimal samples of YH_9 , YH_6 , ThH_{10} , and ThH_9 are also presented for comparison; the red dashed trend line is a fit to these data as described in the text. Horizontal error bars correspond to the lower and upper pressure limits

chamfered cube), containing 14, 24, 29 and 32 vertices, respectively [6, 8].

In the $Fm\bar{3}m$ structure for $n = 3$, the hydrogens form a rhombic dodecahedron with twelve faces of equal edge length d , total surface area $A = 8 \cdot 2^{1/2} d^2$ and distance $\zeta = (6^{1/2}/3)d$ equaling the radius of the inscribed sphere. The $[4^6 6^8]$ polyhedron in $Im\bar{3}m$ structure for $n = 6$ is a truncated octahedron with six square faces of area $A_{\text{sq}} = d^2$, eight hexagon faces of area $A_{\text{hex}} = (3 \cdot 3^{1/2}/2)d^2$ and total surface area $A = (6 + 12 \cdot 3^{1/2})d^2$; the distances measured from the polyhedron center to square face centers $\zeta_{\text{sq}} = 2^{1/2}d$ and $\zeta_{\text{hex}} = (6^{1/2}/2)d$ to hexagon face centers give the area-weighted average $\zeta = (6A_{\text{sq}}\zeta_{\text{sq}} + 8A_{\text{hex}}\zeta_{\text{hex}})/A$.

The $[4^6 5^6 6^6]$ hydrogen polyhedron for $n = 9$ in the $P6_3/mmc$ structure comprises six each

of quadrangles, pentagons, and hexagons. Combining theoretical H sites calculated in [6] and measured lattice parameters in [14] for $P6_3/mmc$ YH_9 , numerical calculations determine $A/d^2 = 31.167$, $\zeta/d = 1.4214$, $C_9 = 0.1260$, and $d/a = 0.3478$, where d is the average of four distinct H-H bond lengths and a is basal lattice parameter. To obtain areas and centroids of the irregular polygons constituting the polyhedral faces, each polygon is divided into triangles based on an edge and an average over polygon edges and vertices is taken. Calculated A and ζ values are uncertain to $\pm 0.03\%$ and $\pm 0.5\%$, respectively, because of nonplanarity in the quadrangle and hexagon polygons. Nearly the same theoretical C_9 values of 0.1263 and 0.1261 are obtained from structural parameter data calculated for CeH_9 and ScH_9 , respectively [6]; C_9 values of 0.1260, 0.1272 and 0.1262 are obtained from the structural data reported for synthesized $P6_3/mmc$ phases of CeH_9 [62], PrH_9 [63], and ThH_9 [16], respectively.

The calculations for $Fm\bar{3}m$ YH_{10} repeat the irregular chambered cube model following the theoretical structure determined in [5, 6, 8]. Owing to its tetragonal structure, $I4/mmm$ YH_4 does not have a hydrogen clathrate structure per se (sites of 18 hydrogens neighboring an Y may be viewed as occupying the vertices of an elongated dodecahedron [7]) and similarly for hydrogens in orthorhombic $Imm2$ YH_7 [15]; from phononic theory, T_C of 87 – 131 and 31 – 46 K are calculated for YH_4 and YH_7 , respectively [15].

2.3 Superconducting MH_n with $M = \text{Y}$ or Th

Other successfully-synthesized hydrogen clathrate compounds, exhibiting superconductivity at high temperatures, include $P6_3/mmc$ YH_9 , experimentally confirmed to have T_C up to 243 K [14] (theoretically up to

276 K [6]) and $Im\bar{3}m$ YH_6 with T_C up to 224 K [14, 15], as well as $Fm\bar{3}m$ ThH_{10} and $P6_3/mmc$ ThH_9 . Discussions of $Fm\bar{3}m$ YH_{10} , which is of special interest because electron-phonon theory predicts T_C above room temperature (303 – 326 K [5, 6, 8, 21]), and CaH_6 in the seminal prediction [1] are included in Section 3.1 as potentially superconducting MH_n materials.

Of the various YH_n clathrates predicted to be superconductors according to Migdal-Éliashberg theory [5-9, 15, 21, 64], the experimentally verified superconducting syntheses (YH_3 is non-superconducting at experimental pressures [14, 65-67]) include yttrium polyhydride mixtures comprising phases of YH_4 , YH_6 , YH_7 , and YH_9 [14, 15]. For $P6_3/mmc$ YH_9 , maximum $T_C = 243$ K at $P = 201$ GPa is reported in [14] (sample 2 containing remains of YH_6 and traces of YH_4) with corresponding lattice parameters $a = 3.406$ Å and $c = 5.210$ Å, and mean H-H distance $d = 1.185$ Å in the theoretical H_{29} polyhedron [6]. Phonon theory predicts $T_C = 255 - 276$ K at $P = 150$ GPa [6]. Using $C_9 = 0.1260$ from Table 2 and $\sigma = 6$, Eq. (6) yields $T_{C0} = 274.4$ K, which is a hypothetical value in view of predictions of cationic Y [6-8]. Owing to inter-reservoir charge imbalance, $P6_3/mmc$ YH_9 is expected to have an intrinsically non-optimal and depressed superconducting transition. A close analogy is found in the compressed A_3C_{60} superconductors, where $T_C < T_{C0}$ occurs systematically for alkali constituents A other than pure Cs [27, 41]. The 11% reduction of T_C from T_{C0} for $P6_3/mmc$ YH_9 may be interpreted as a pair breaking effect (see, e.g. Eq. (4) in [41]) with pair-breaking energy $\alpha_p = 0.12 k_B T_C$ originating from excess charge in the type I H_9 reservoir. Expressing α_p as a fraction $f \approx 0.12$ of Planckian dissipation ($\sim k_B T_C$ at T_C), which is related in turn to the excess charge fraction as $f \approx \delta/\sigma$, one obtains from $\delta = \sigma f$ an

estimated excess charge of $\sim 0.7e$ per H_9 . Theoretical charge transfer from Y to the H cage calculated for $P6_3/mmc$ YH_9 [6], predicting cationic Y, is evidently contrary the idea of a balanced allocation of 12 valence electrons between Y and H_9 . Band structure results for YH_6 , YH_9 , and YH_{10} in [6] (Fig. S14 caption) also show that H-projected orbitals dominate the density of states near the Fermi level.

In the case of $Im\bar{3}m$ YH_6 , a range $a = 3.529 - 3.582$ Å in bcc lattice parameters is measured at pressures from 201 down to 165 GPa in samples containing YH_6 [14, 15], corresponding to theoretical average nearest-neighbor H-H distances of $d = 1.248 - 1.266$ Å between the 24 hydrogens at the vertices of a truncated octahedron structure [6]. The optimal superconducting state requires the charge fraction given by Eq. (3) of $\sigma = (6 + 3)/2 = 4.5$. From Eq. (6) with $C_6 = 0.1525$ (Table 2), the corresponding calculated optimal T_{C0} is 252 – 265 K. Experimental results for samples denoted as YH_6 are $T_C = 210 - 227$ K (statistically $T_C = 219 \pm 6$ K) [14, 15] and for samples comprising YH_6 and other phase material, results are $T_C = 214 - 243$ K ($T_C = 226 \pm 12$ K). Predictions from Migdal-Éliashberg theory vary over a broad range, $T_C = 158 - 301$ K for P ranging from 350 down to 100 GPa [6-9, 14] (Section A1). The $\sim 13\%$ discrepancy between T_{C0} predicted by Eq. (6) and measurements of T_C are attributed to several factors. Most fundamental is the expected deviation from charge equilibrium, owing to ionic charge transfer from Y to H_6 , as deduced from band structure results. Partially displayed PDOS curves for $Im\bar{3}m$ YH_6 in [6,8] (limited to $E \geq -20$ eV) show occupation of Y- d orbitals, but these published data are insufficient for determining relative Y and H_6 projected charges and whether charge allocation in YH_6 is theoretically balanced. However, the findings reported in [7] are that

Table 3 Normalized normal-state-resistance temperature slope S of samples comprising MH_n (one or more phases) from published resistance-vs.-temperature curves. Tabulated are reference number, MH_n compound(s), sample identification number, reference figure number and curve color, transition temperature T_C , pressure P , and S

Expt. Ref.	MH_n	Sample number	Figure	T_C (K)	P (GPa)	S
[12]	LaH ₁₀ , LaH ₋₁₂	3	1 – blue	249	159	1.08
[12]	LaH ₁₀ , LaH ₋₁₂	3	2 (a)	250	–	0.91
[12]	LaH ₁₀	1	4 – black	249	151	0.62
[13]	LaH ₁₀	A	1 – blue	262	188	1.06
[13]	LaH ₁₀	A	1 – red	248	196	2.8
[15]	YH ₆ , YH ₄	K1	5 (a)	224	166	0.46
[15]	YH ₆ , YH ₇	K1	5 (b)	218	165	0.96
[14]	YH ₆ , YH ₄	2	1 (a) – blue	227	201	0.37
[14]	YH ₉ , YH ₆ , YH ₄	2	1 (a) – red	243	201	1.01
[14]	YH ₄ , YH ₆	5	1 (d)	214	160	0.05
[16]	ThH ₉	M2	5 (b)	146	170	0.39
[16]	ThH ₁₀	M3	5 (a)	159	174	0.18
[16]	ThH ₁₀ , ThH ₉		S31 (b)	161	170	0.34
[56]	H ₃ S	11/2018	1	201	155	0.93

each H atom accepts $0.2e$, effectively precluding anionic character of the Y ion. The other factor, extrinsic to experiment, is the admixture of phases other than YH₆; the samples reported in [14, 15] contain variously $I4/mmm$ YH₄, $Im\bar{3}m$ YH₆, $Imm2$ YH₇, $P1$ Y₂H₁₅, and an unidentified crystalline form. Multiple phases render the task of ascertaining the actual superconducting component(s) rather ambiguous.

For $Fm\bar{3}m$ YH₃, which theoretically supports superconductivity [64, 65] but is thus far found to be a normal metal above 5 K [14], integrated electron density analysis indicates acquisition of $1.56e$ charge on H₃ at $P = 120$ GPa (and similarly for $I4/mmm$ YH₄) [7]. Adherence to $3e$ on both Y and H₃ would entail hybridization of H $1s^1$ and Y $4d$ -like orbitals such that the charge on Y is effectively $3e$.

Of the synthesized ThH_n compounds for $n = 4, 6, 9$ and 10 reported in [16], the two found to be superconducting are $P6_3/mmc$ ThH₉ with T_C of 146 K (170 GPa) and $Fm\bar{3}m$ ThH₁₀ with T_C of 159 – 161 K (170 – 174 GPa). In the case of $Fm\bar{3}m$ ThH₁₀, the Éliashberg equations are cited [10], predicting T_C of 206 – 227 K at 174 GPa,⁴ significantly higher than the measured value. Descriptions of the samples presented in [16] indicate mechanical distortion and inclusion of other Th-hydride phases, including ThH₄. Temperature dependences of the samples' resistances shows marked departure from proportionality to T in the normal state, exhibiting instead large extrapolated residual resistance as ratios $R_N(0)/R_N(T_C)$ of 0.61 –

⁴ Also presented in [16] are results of calculations for $P6_3/mmc$ ThH₉ from the Allen-Dynes formula extrapolated to 170 GPa, predicting T_C of 125 – 147 K. For $Fm\bar{3}m$ ThH₁₀, the Allen-Dynes formula yields 160 – 193 K [10, 16].

0.82 (Section A2, Table 3), which is a common symptom of non-optimal superconducting material. For example, H_3S prepared without room-temperature annealing exhibits a suppression of T_C (< 200 K) that correlates with increased residual resistance [41]. As superconductors, ThH_9 and ThH_{10} may also be intrinsically non-optimal with respect to equilibrium between charges associated with Th and H_n . Unfortunately, available information on the electronic structure of ThH_9 and ThH_{10} [10, 16] is insufficiently complete for quantifying allocation of the valence charges, although H-projected bands calculated for $Fm\bar{3}m$ ThH_{10} appear to dominate the electronic band structure reported in [10]. Counting the $6d^27s^2$ electron configuration of Th as valence $v = 4$, giving $\sigma = (4 + n)/2$, values of hypothetically optimal T_{C0} ($> T_C$) are determined from Eq. (6) and Table 2 using experimentally measured lattice parameters. For $P6_3/mmc$ ThH_9 , $C_9 = 0.1260$, $\sigma = 6.5$, $d = 1.269 - 1.338$ Å, and $T_{C0} = 224 - 249$ K ($P = 86 - 172$ GPa, Table S4 in [16]) and for $Fm\bar{3}m$ ThH_{10} , $C_{10} = 0.1067$, $\sigma = 7$, $d = 1.185 - 1.231$ Å, and $T_{C0} = 232 - 251$ K ($P = 85 - 183$ GPa, Table S5 in [16]), noting that d relates inversely to P .

The above experimental values of T_C for YH_6 , YH_9 , ThH_9 , and ThH_{10} are shown in Fig. 2 as functions of $(\ell\zeta)^{-1} \equiv C_n \sigma^{1/2}/d^2$, where the symbols denote averages and error bars correspond to ranges in T_C and d . Results for these non-optimal samples suggest the trend indicated by the dashed line, a linear fit intercepting the solid line for T_{C0} at 293 ± 6 K.

3 Discussion

The curious absence of superconductivity in seemingly promising $M\text{H}_n$ materials is considered in Section 3.1 from the perspective of charge balance, disorder, and phase purity. The suppressed T_C reported for fcc LaD_{10} in

determining the H-D isotope effect [12] is considered in Section 3.2 in terms of materials issues [36], which are shown to be relevant for interpreting the T_C of D_3S [42] and the oxygen isotope effect in high- T_C cuprates [68-70]. A study to detect the signature of the charge transfer potential e^2/ζ embedded in Eq. (1) by optical reflectivity, similar to its successful use in several high- T_C materials, is proposed for LaH_{10} in Section 3.3, and coexisting electron-phonon and M -H electronic Coulomb interactions are contemplated for the case of LaH_{10} in Section 3.4.

3.1 Potentially Superconducting Superhydride Clathrates

Virtually all binary superhydrides, except those showing weak coupling [6, 62, 63], are predicted from electron-phonon theory to be superconducting with high transition temperature under high pressure (e.g., [1-10, 15, 20-26]). While a few have been successfully synthesized and shown to be superconducting, an unknown number may have been synthesized but found not to have the predicted high T_C or are non-superconducting. Still others, like $Fm\bar{3}m$ YH_{10} , are awaiting to be synthesized [14], or have failed to be synthesized. Accepting that synthesis issues persist in some cases, it is proposed that the superconducting condensate quality in binary clathrates is determined by the chemical details of the enclosed atom and inter-reservoir charge equilibrium. The $Fm\bar{3}m$ binary structure YH_{10} is particularly noteworthy, owing to predictions of T_C exceeding 300 K at high pressures [5, 6, 8, 21], although it has yet to be synthesized [14].

Like its LaH_{10} counterpart, $Fm\bar{3}m$ -phase YH_{10} is expected to contain an H_{32} cage in the form of an irregular chamfered cube. Viewing the electronic structure of LaH_{10} as the benchmark model, one may consider that the 3

valence electrons of La, forming La-H hybridized states with the native 10 electrons from H, favorably produce $(13/2)e$ charge in La-projected orbitals and equal charge on H_{10} . Equal allocation is enabled by the $4f$ atomic orbitals of La that are otherwise unoccupied. For YH_{10} , theoretical PDOS at 250 GPa plotted in Fig. S3(c) of [5] shows occupied s , p , d , and f orbitals projected onto Y, as would be necessary in forming anionic Y. Estimated integrations of PDOS curves over the energy range $-1.5 \text{ Ry} < E < E_F$ indicate electron charges of $5.4e$ in Y orbitals and $6.7e$ in H s - p orbitals, which are in the ratio 1.24. The total of $12.1e$, falling short of the expected 13, suggests that $0.9e$ is uncounted, rendering the ratio uncertain. The calculated band structure diagram plotted in Fig. 2 of [8] employs colored tones to show projections onto Y or H states, qualitatively indicating that the charges on H_{10} relative to Y are in ratio of about 1.3. Although charge allocation is not well elucidated by these methods, the band structure results in [5] do find anionic charge on Y and, moreover, that the total charge on H_{10} is just 3% above the optimal value of $6.5e$ corresponding to $\sigma = 6.5$. Calculations at a different pressure could change indicated charge imbalance, although convex hull diagrams of formation enthalpy predict that YH_{10} is stable for $P > 250 \text{ GPa}$ [5] or $P > 225 \text{ GPa}$ [8]. The theoretical uncertainty therefore doesn't rule out synthesizing YH_{10} with H_{10} charge close to the optimal $6.5e$ near the theoretical pressure range of 225 – 300 GPa for stability [5, 8]. Assuming the theoretical values for lattice parameter $a = 4.600 - 4.747 \text{ \AA}$, average H-H spacing $d = 1.070 - 1.105 \text{ \AA}$, and H-H bond-length ratio $r = 1.09$ [8], application of Eq. (6) and Table 2 evaluates to $T_{C0} = 278 - 296 \text{ K}$ for $Fm\bar{3}m$ YH_{10} . Thus, inter-reservoir Coulomb interactions may be considered as a viable mechanism for superconductivity near room temperature in a compressed YH_{10} clathrate.

In the search for high-temperature superconductivity, some researchers have considered other metal-superhydride clathrates as promising candidates, calculating T_C at various high pressures based on strong electron-phonon Éliashberg-based theories [1, 2, 5, 6, 8, 10, 14, 16, 21, 62, 63, 71-73]. Of the superhydrides synthesized with rare earth M [62, 63, 74, 75], no superconductivity for $M = \text{Ce}$ has been reported [62, 74], and for $M = \text{Pr}$, emergence of T_C below 9 K is reported [63]. Achieving optimal high- T_C superconductivity, mediated by M -H Coulomb interactions in these and other MH_n clathrates, is contingent on there being an optimal charge allocation between the two charge reservoirs. Verification of Eq. (6) for these other MH_n clathrates awaits the successful stabilization of optimal superconducting syntheses.

Assuming strong electron-phonon interactions, a sodalite-like CaH_6 phase with bcc Ca and truncated octahedron H_{24} cage is predicted from strong-coupled phonon theory to be superconducting in the range $T_C = 220 - 235 \text{ K}$ at a pressure of 150 GPa [1]. More recent studies predict superconductivity in CaH_n with higher H content. Two examples are the $C2/m$ phase CaH_9 ($T_C = 240 - 266 \text{ K}$, $P = 300 \text{ GPa}$) and $R\bar{3}m$ CaH_{10} ($T_C = 157 - 175 \text{ K}$, $P = 400 \text{ GPa}$) [71]. To date, however, no observation of superconductivity in Ca hydrides has been reported and it is uncertain as to whether these materials have even been successfully synthesized. The Ca is evidently a cation in CaH_6 , owing to a charge transfer to H_6 calculated to be $1.02e$ [1]. Integration of the PDOS shown in Fig. S16 in [1] over the range $-20 \text{ eV} \leq E \leq E_F$ (excludes core states for $E < 20 \text{ eV}$) yields a charge of $2.45e$ on Ca and $5.54e$ on H_6 . Compared to the optimal $\sigma = 4$ from Eq. (3) with $n = 6$ and $\nu = 2$, the H_6 reservoir is predicted to be overdoped by $1.54e$. Cation Ca is also predicted for CaH_9 and CaH_{10} , owing to Ca-to-H charge transfer [71]. Thus, these CaH_n clathrate systems are

intrinsically non-optimized, owing to an imbalance of charge between the type II Ca and type I H_n reservoirs, which, with synthesis kinetics and other clathrate system complexities, could explain the absence of a successfully synthesized CaH_n superconductor.

3.2 Deuteride Phases: LaD_{10} , D_3S

Measurement of the H-D isotope effect in $Fm\bar{3}m$ LaH_{10} could provide important information regarding the role played by phonons in the formation of the superconducting state. An H-D mass isotope effect exponent $\alpha = 0.48$ is calculated for $P = 200$ GPa in [23] from the formula for T_C in Allen and Dynes [19] and $\alpha = 0.43$ for P around 160 GPa in [15]. The available data are the resistance transitions shown in Fig. 4 of [12] for LaH_{10} and LaD_{10} samples, showing $T_C = 249$ K at 151 GPa and 180 K at 152 GPa, respectively, seemingly implying $\alpha = 0.46$. Transition midpoint temperatures are lower than T_C by $\Delta T_C \approx 7$ and ≈ 14 K, respectively. However, the value of α obtained in this manner may not be intrinsic, but rather related to the width of the resistance transition for the LaD_{10} sample since $\alpha \approx 6 \Delta T_C/T_C$, which curiously has the same factor found for several samples of D_3S , wherein $\alpha = (5-7) \Delta T_C/T_C$ [42]. Such correlations between mass isotope exponents and widths of superconducting transitions have been observed previously in cuprates [68], where the oxygen mass isotope effect exponent bears the relation $\alpha_O \approx 3 \Delta T_C/T_C$ for samples of $Y_{1-x}Pr_xBa_2Cu_3O_{7-\delta}$ (here, ΔT_C is the temperature interval corresponding to 10% and 90% of full transition [68]). Anomalous behavior apparent in α_O is attributed to disorder in non-optimal samples [69, 70]. Taking the various levels of disorder into account, the T_C data for the D_3S and H_3S samples studied in [57] has

the corrected exponent value of $\alpha = 0.043 \pm 0.140$ [42], indicating an inconsistency with phonon mediation and necessitating a more unconventional, Coulomb-based approach to the superconductivity in H_3S [41]. The materials issues clearly evident with synthesizing D_3S are not considered in the theoretical treatments regarding the originating superconducting mechanism reviewed in [76]. The observed resistance drop temperatures are deemed inconclusive for an isotope effect that may or may not be present [4].

3.3 Interlayer Coulomb Interaction Potential

Optical reflectivity data can provide a direct experimental test for the interlayer Coulombic pairing interaction potential e^2/ζ imbedded in the expression for T_{C0} in Eq. (1), as discussed in [41] and [49]. In compressed A15-phase Cs_3C_{60} (1.8 GPa pressure), a maximum in the vicinity of 2500 cm^{-1} (0.31 eV) is found in the room-temperature mid-infrared component of the optical conductivity obtained from Kramers-Kronig analysis of ambient-temperature reflectivity (Fig. 1I in [77]), and in compressed H_3S (150 GPa pressure), a dip near 0.46 eV is observed in the normal-state reflectivity (Fig. 4a in [78]). These energies are shown to be proportional to ζ^{-1} in [41] and can be calculated from the expression $[1.0(1) \text{ eV } \text{\AA}] \zeta^{-1}$. A mid-infrared signature near 0.6 eV can, therefore, be projected for $Fm\bar{3}m$ LaH_{10} , e.g. from normal-state reflectance measurements, by conjecturing the same ζ^{-1} scaling with ζ in the range $1.728 - 1.828 \text{ \AA}$ determined from cell volume data in [12, 13]. A different optical signature, that of phonons, is proposed in [79] from theoretical temperature dependence of the reflectivity in the superconducting state; it is notably absent above T_C .

Given the compelling arguments put forth in [41] comparing A15 Cs_3C_{60} and $\text{Im}\bar{3}m \text{H}_3\text{S}$, measurement and analysis of mid-infrared reflectivity in LaH_{10} (or other hydrogen clathrates) seem an imperative in correctly determining the origin and nature of the pairing mechanism.

3.4 Coexisting Phonon/Coulomb Interactions – LaH_{10}

Of the recent advances in computational theoretical methods, especially noteworthy are results in [5, 6], which have predicted the synthesis of $\text{Fm}\bar{3}m$ -phase LaH_{10} [11-13] and also anticipated the superconductivity above 260 K reported in [13]. Calculations of T_C in [5, 6], reaching as high as 286 – 288 K, bear close correspondence to experimental evidence of onset superconductivity at high temperatures in [13, 29]. Combined with subsequent theoretical results in [22-26], phonon mechanisms seemingly appear capable

of addressing the full experimental ranges in T_C and P reported in [12, 13], given that the body of wide-ranging theoretical results overlap available data, as illustrated in Section A1 (Figs. 3–4). Data in [13] indicate $T_C \in (240, 282)$ K and occurring within the range $P \in (179, 202)$ GPa, suggesting a strong pressure dependence with mean slope $+1.9(6)$ K/GPa, similar to $+2.4(4)$ K/GPa by fitting data reported in [29] (see Fig. 10 therein). On the other hand, data in [12] comprise $T_C \in (243, 251.5)$ K and $P \in (140, 218)$ GPa forming the “dome” with essentially zero (-0.02 ± 0.02 K/GPa) average slope. The clearly conflicting pressure dependences from these two studies are pointed out in [4] as suggestive of different phases (discrepancies in phase and stoichiometry of the samples studied in [12, 13] do indicate the presence of non-optimal material). However, there is no conflict related to the optimal phase found from each study, where the results for optimal T_C and P (Table 1) are connected by the same

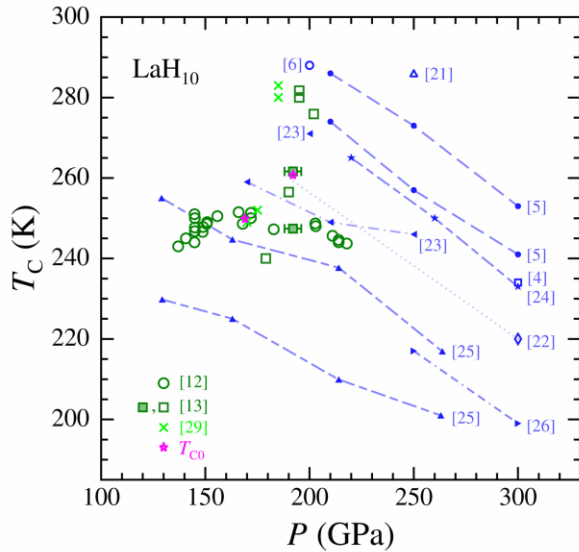


Fig. 3 Plot of transition temperature T_C vs. pressure P for $\text{Fm}\bar{3}m \text{LaH}_{10}$ (marked with source references). Larger green symbols denote experimental data from [12, 13, 29]; smaller blue symbols and connecting lines represent theoretical results from [4-6, 21-26]. Magenta star symbols are at T_{C0} and P as given in Table 1

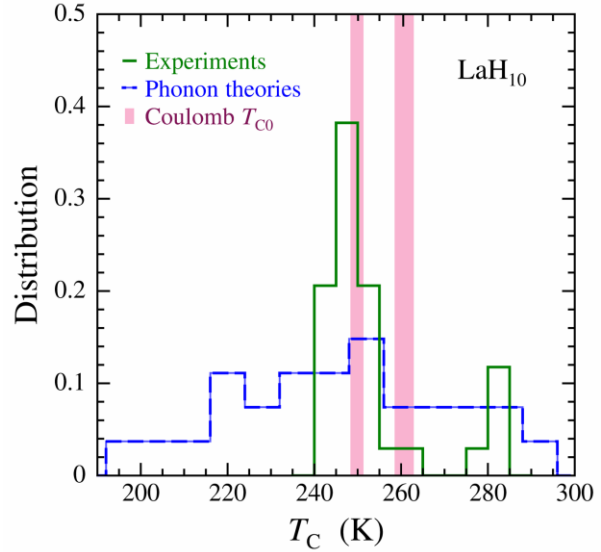


Fig. 4 Distributions of experimental and theoretical results for T_C of $\text{Fm}\bar{3}m \text{LaH}_{10}$, as presented in Fig. 3 and Table 1. Normalized histograms show distributions in T_C from experiments (solid green) and phonon theories (dashed blue). Vertical pink bars denote T_{C0} presented in Table 1 (bar width denotes uncertainty)

La-H electronic Coulomb interaction (Eq. (1) and Fig. 2).

The combination of the dissonant phonon-based theoretical $T_C(P)$ results with the accordant Coulombic-based findings of Eq. (1) for optimal $T_C = T_{C0}$ augurs well for a comprehensively applicable treatment, even though various mathematical approximations, assumptions, and rigor have thus far been limited to essentially conventional electron-phonon calculations of T_C [4-6, 22-26]. To this end, the interplay between the inter-reservoir Coulomb interactions underlying Eq. (1) with phononic mechanisms may be considered. Non-optimal superconducting phases are manifested mainly as different temperatures relative to the optimal T_C in [13] and by different pressures relative the optimal P in [12]. Optimal T_C , therefore, denotes a superconducting-phase fixed point that is determined by the electronic La-H interactions. Shallowness of the T_C -vs.- P dome in LaH₁₀ (< 4% variation in T_C) suggests that superconductivity in the non-optimal material may be complimented by sufficiently strong electron-phonon coupling [25], given that variations of T_C with pressure in A15-phase Cs₃C₆₀ [27] or doping in cuprate superconductors [31] are comparatively larger by an order of magnitude. Coexistence of Coulombic and phononic mechanisms in non-optimal material might be observable. Possible evidence to consider is the broad resistance drop near 225 K for sample 3 of LaH₁₀ in [12] (Fig. 1, blue curve), where $T_C = 249$ K and $P = 150$ GPa are both less than the optimal values in Table 1. It is also worth noting that a possible source of at least some of the phonon-related phenomena in LaH₁₀ may be a sympathetic response of the lattice to the formation of the Coulomb-mediated superconducting state, as suggested for Cs₃C₆₀ [49]. At present, more definitive evaluations of electronic Coulomb interactions, electron-phonon mechanisms, and their interplay await

more extensive experimental study. Contributions of interlayer Coulomb interactions to conventional electron-phonon superconductivity are treated for electronically layered structures in [80].

4 Conclusion

Available experimental data on LaH₁₀ and YH₉ samples contain persuasive evidence of unconventional high- T_C superconductivity in these compounds, including a maximum in $T_C(P)$ [12, 14], suggesting optimization, and a linear temperature dependence in the normal-state resistance [30], which places upper bounds on the electron-phonon coupling strength, owing to the absence of resistance saturation [43]. Although theory based on phonon mediation notably predicted superconductivity at high temperatures [5, 6], convergence of broad ranges in calculated T_C to experimental values is hampered by theoretical pressure dependences [5, 24-26] that are contrary to experiment [29], thus necessitating an alternate approach.

Examination of theoretical band structure shows that $\sigma = (v + n)/2$ holds for $Fm\bar{3}m$ LaH₁₀, owing to the anionic nature of the La ion [22]. However, theory for $P6_3/mmc$ YH₉ [6] indicates that cationic Y forms H₉-related charges exceeding the optimal $\sigma = 6$, and similarly for $Im\bar{3}m$ YH₆ and $Fm\bar{3}m$ YH₁₀ [6-8]. When optimal charge equilibrium is intrinsically unrealizable, the experimental T_C is expected to be suppressed relative to T_{C0} . For $Fm\bar{3}m$ LaH₁₀, optimal transition points T_C of 251(1) K and 262(1) K at optimal pressures of 169(4) and 192(4) GPa are identified from results in [12] and [13], respectively. The corresponding calculated T_{C0} values are 249.8(1.3) and 260.7(2.0) K, respectively, which compare extremely well (with a < 2 K uncertainty) with experimental values. For $P6_3/mmc$ YH₉, the highest experimental T_C of 243 K in a mixed-phase sample is depressed

by 11%, attributable to an overdoped H-cage; the phononic theory prediction is 255 – 276 K [6]. Transition temperatures reported for nominally YH_6 mixed-phase samples [14, 15], and for ThH_9 and ThH_{10} [16] samples with large residual resistances, fall short for either optimal Coulomb interactions or phonon interactions. Comparison of theory to experiment is, unfortunately, clouded by the ambiguities of interpreting mixed phase samples and suppression of T_C by intrinsic deviation from $M\text{-H}_n$ charge equilibrium, found theoretically for $M = \text{Y}$, and extrinsic effects of sample disorder, notably for $M = \text{Th}$.

Mass isotope data for DH_{10} reported in [12], deemed inconclusive in [4], are shown to more likely reflect the inverse correlation between T_C and the fractional transition width $\Delta T_C/T_C$, as is found for D_3S . Consequently, and notwithstanding the predictions of Éliashberg theory, the precise role played by phonons in the superconductivity of $M\text{H}_n$ awaits further investigation. Since quantitative scaling with the theoretical e^2/ζ is noted from optical evidence for compressed $\text{A15 Cs}_3\text{C}_{60}$ [49] and H_3S [41], and plausibly extending to LaH_{10} , reflectivity measurements of $M\text{H}_n$ may prove invaluable in determining the nature of the mediating boson.

Acknowledgments The authors are grateful for support from the College of William and Mary, New Jersey Institute of Technology, and the University of Notre Dame. We also acknowledge helpful information provided by Dr. F. Peng.

Funding Information This study was supported by Physikon Research Corporation (Project No. PL-206) and the New Jersey Institute of Technology.

Compliance with Ethical Standards

Conflict of Interest The authors declare that they have no conflict of interest.

Appendix

The following appendix sections present and analyze results for the pressure variation in T_C , normal-state resistance, pressure dependence of the lattice parameter, and accuracy and systematic error of the model, based on this work and published data.

A1 Pressure Variation in T_C

A comprehensive plot of available experimental data [12, 13, 29] and theoretical results [4-6, 21-26] pertaining to the variation of T_C with pressure P in LaH_{10} is presented in Fig. 3. Open circle symbols shown for $P \in (140, 218)$ GPa and $T_C \in (243, 251)$ K are transcriptions of experimental data from Fig. 1 inset of [12] (error bars omitted for clarity). The arched trend in T_C vs. P , noted in [12], comprises points with highest T_C at 251.5 and 251.3 K (error bars ± 1 K) corresponding to P at 166 and 172 GPa (± 2 GPa), respectively (data for sample 5 in [12]). Taking rounded averages and uncertainties, the values 251(1) K and 169(4) GPa thus determine the experimentally measured optimal T_C and P , respectively, shown in the first row of Table 1.

Although experimental measurements of T_C are not specified in [13], full superconducting resistance transition curves for cooling and warming of sample A are presented in Fig. 3 therein. Onset values of T_C are determined herein to about ± 1 K uncertainty from the intersection of tangents drawn through the linear-in-T normal-state region (see Section A2) and the more steeply sloped region just below the transition onset. This method yields T_C of 262(1) and 247(1) K for cooling and warming, respectively, and is shown as the filled square symbols in Fig. 3,

where horizontal error bars span the pressures of 188 and 196 GPa associated with the data (i.e. $P = 192 \pm 4$ GPa). The higher T_C for cooling is assumed to be closer to optimal and therefore entered in the second row of Table 1. Coincidentally, Fig. 3 shows by way of comparison that the onset T_C for warming lies in the region of the lower T_C observed in the data from [12] (sample 6 therein). Other resistance-*vs.*-temperature data in [13] show resistance drops suggesting onsets of superconducting behavior (full transitions not displayed). Figure 4 in [13] shows a resistance drop at 280 K for 0.1 mA applied current and 195 GPa pressure for sample F. Figure S4 in [13] shows drops at 257, 282, and 276 K for pressures of 190, 195, and 202 GPa, respectively, for sample B. Additionally, a small jump at 240 K (at assumed 179 GPa) is described for sample G [13]. The five open square symbols in Fig. 3 represent these other temperatures and pressures drawn from [13]. Cross symbols represent data from Fig. 10 of [29].

Small symbols in Fig. 3 display results of theoretical calculations of T_C for LaH_{10} from strong electron-phonon coupling based on Migdal-Éliashberg theory, density functional theory or *ab initio* methods (labels distinguish the source references [4-6, 21-26], exclusive of ranges in theoretical stability study of [81]). Results calculated at multiple values of P , connected by broken lines, show that the electron-phonon mechanism reproducibly predicts that T_C has a monotonically decreasing dependence on P with average slope $\Delta T_C/\Delta P \approx -0.30 \pm 0.08$ K/GPa [5, 23-26], a finding with theoretical basis [26]. The dotted line in Fig. 3 illustrates the linear extrapolation from the calculated point (diamond symbol) to the range of experimental pressure that is used in [22]. Superconducting density functional theory (SCDFT), as applied in [23], predicts $T_C = 271$ K at $P = 200$ GPa, whereas SCDFT applied in

[25] predicts a much lower $T_C = 214$ K (interpolated to $P = 200$ GPa).

The magenta star symbols in Fig. 3 are the results for T_{C0} given in Table 1 at the values of P indicated. These two points define a positive change $\Delta T_C/\Delta P = +0.47$ K/GPa, in contrast to negative variations predicted in electron-phonon theory [5, 22, 24-26].

The distributions of the T_C values from Fig. 3 are cast in Fig. 4 in the form of histograms corresponding to the experiments (solid green) and phonon theories (dashed blue) normalized to the number of points (30 and 27, respectively), and with bin sizes of 5 K and 10 K, respectively. Statistical averages and \pm standard deviations of the distributions are as follows: $T_C = 251 \pm 10$ K (experiments) and 245 ± 26 K (phonon theories); $P = 174 \pm 27$ GPa (experiments) and 232 ± 52 GPa (phonon theories). Theoretical pressure dependence suggests shifting the statistical

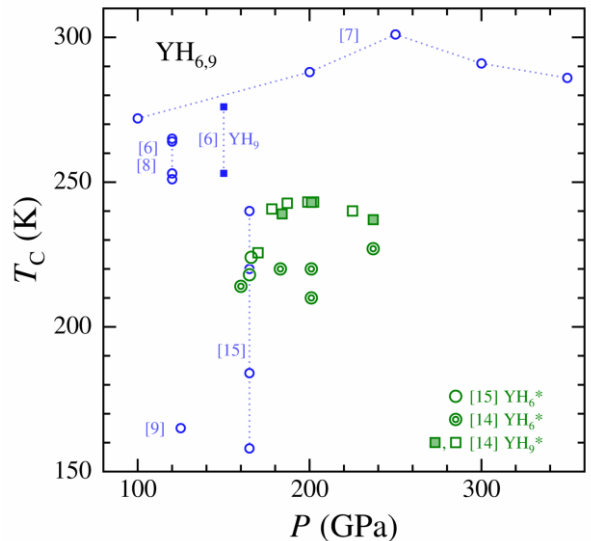


Fig. 5 Plot of transition temperature T_C vs. pressure P for $Im\bar{3}m$ YH_6 and $P6_3/mmc$ YH_9 (marked with source references), denoted by circular and square symbols, respectively. Larger green symbols denote experimental data [14, 15]; smaller blue symbols and connecting lines represent phonon theories [6-9, 15]

average for the phonon theories as $T_C = 263 \pm 29$ K at $P \rightarrow 174$ GPa. Pre-experimental theories include predictions of 274 and 286 K at 210 GPa in [5] and 288 K at 200 GPa in [6], which may be compared to resistance drops [13] or magnetic onsets [29] at temperatures of 276 – 283 K and pressures of 185 – 202 GPa, and represented by the smaller histogram fragment in Fig. 4. The two pink vertical bars (and widths) in Fig. 4 represent the values of T_{C0} (and uncertainties) given in Table 1.

Figure 5 is a comprehensive plot of T_C vs. P for YH_6 (circle symbols) and YH_9 (square symbols) where the larger green circles and squares denote experimental data in [14, 15]. The smaller blue circles and filled squares denote theoretical results for YH_6 [6-9, 14] and YH_9 [6], respectively. Asterisk symbols in the legend express the caveat that phases other than those indicated are determined from X-ray data analysis (e.g. YH_4) [14]. Statistical averages and \pm standard deviations of samples identified as YH_6 in [14, 15] are $T_C = 219 \pm 5$ K and $P = 188 \pm 28$ GPa; statistics for the YH_6 phonon theories are $T_C = 245 \pm 47$ K and $P = 176 \pm 75$ GPa. The “dome” trend in T_C vs. P for YH_9 with maximum $T_C = 243$ K at $P = 201$ GPa is noted in [14] (filled symbols, before change in P ; open symbols, after change in P); phonon theory predicts $T_C = 253 - 287$ at $P = 150$ GPa [6].

A2 Normal State Resistance

Unique features signifying unconventional high- T_C superconductivity are a linear temperature dependence in the normal state resistivity, $\rho_N(T) \propto T$, and the absence of saturation at high temperature, such that the negative curvature of $\rho_N(T)$ for conventional strong electron-phonon coupled metals is absent [43]. Such unconventional behavior in $\rho_N(T)$, observed in optimally- and over-doped high- T_C cuprates, is ascribed generally to

“Planckian” dissipation phenomena [44, 45]. Superconducting LaH_{10} and YH_9 are exemplary of this behavior for $T > T_C$, as can be seen in Fig. 6 showing resistance vs. temperature for (a) $Fm\bar{3}m$ LaH_{10} sample 3 from Fig. 1 of [12] (blue curve, $P = 150$ GPa, $T_C \sim 249$ K) and (b) $P6_3/mmc$ YH_9 sample 2 from Fig. 1a of [14] (red curve, $P = 201$ GPa, $T_C = 243$ K). Dotted lines illustrate linear dependence for $T > T_C$ extrapolating to the origin. Resistance of LaH_{10} sample A in [13] (Fig. 3 therein, cooling curve) and $Im\bar{3}m$ YH_6 sample M1 in [15] are also consistent with normal-state linearity in T . Table 3 summarizes normalized normal-state slopes obtained from the temperature dependence of the resistance $R_N(T)$ reported for various samples of La, Y, and Th superhydrides and H_3S , defined as $S = [T_C/R_N(T_C)] (\Delta R_N/\Delta T)$ in terms of slope $\Delta R_N/\Delta T$ taken asymptotically

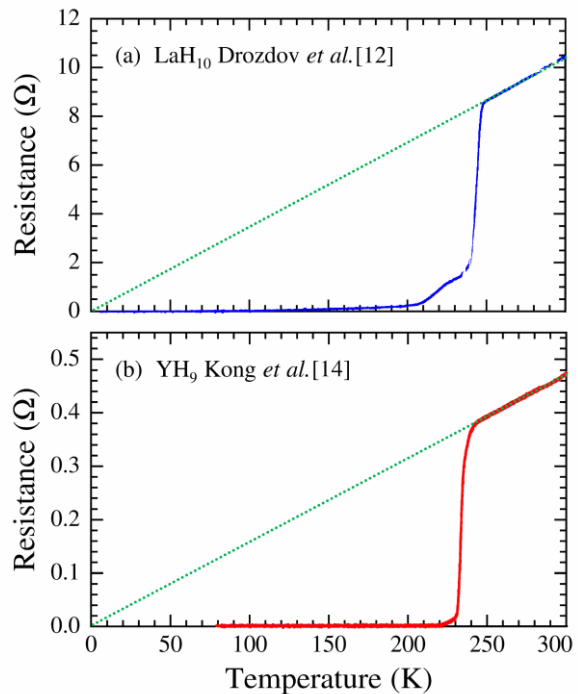


Fig. 6 Resistance vs. temperature for (a) $Fm\bar{3}m$ LaH_{10} sample 3 from Fig. 1 of [12] (blue curve) and (b) $P6_3/mmc$ YH_9 sample 2 from Fig. 1(a) of [14] (red curve). Dotted lines show extrapolations of normal-state resistance to the origin

above T_C and $R_N(T_C)$ as extrapolated to T_C . Resistance in applied magnetic fields, which depress the superconducting transition, shows linear-in- T extending to $T < T_C$; $S = 0.91$ at 9 Tesla is obtained for sample 3 from Fig. 2 (a) in [12] and extension to above 60 Tesla is reported in [30]. Extrapolated residual resistance ratio is given by $R_N(0)/R_N(T_C) = 1 - S$. The statistical distribution in S with bin size 0.25 is shown in Fig. 7 (from Table 3 and near unity S assumed from [30]), indicating that highest probability occurs at $S \approx 1$. Ideally, S approaches unity for (unconventional) optimal high- T_C superconductors.

Dissipation from inelastic electron scattering in the normal state is determined from the scattering rate formula $\tau_N^{-1} = \rho_N e^2 n/m$, written in terms of density n and mass m of the carriers. An estimated $\rho_N \sim 10^{-5} \Omega \text{ cm}$ at $T \approx 285 \text{ K}$ is calculated for sample F in [13] from measured resistance $\approx 0.11 \text{ m}\Omega$ at 0.1 mA indicated in Fig. 4, thickness $\sim 2 \mu\text{m}$ mentioned in the supplemental material of [13], and an assumed Van

der Pauw factor of 4.53. Carrier density n is obtained from the charge fraction $\sigma = 6.5$ associated with H_{10} ($6.5e$ per formula unit volume), m is derived from theoretical superconducting parameters as $m = \hbar k_F/v_F = \hbar^2 k_F/\pi \Delta \xi$ with theoretical gap $\Delta = 2.3 k_B T_C$ [22] and experimental coherence distance $\xi = 1.7 \text{ nm}$ (average determined in [12]); Fermi wave vector is determined as $k_F = (3\pi^2 n/g)^{1/3}$ with $g = 2$ (approximating the theoretical Fermi surface in [22] as two equal-area spheres). The Planckian dissipation energy evaluates to $\hbar \tau_N^{-1} \sim 4k_B T$ from the above data for LaH_{10} . Acknowledging that this analysis provides only a single order of magnitude estimation, the dissipation may be considered as similar to $(1.3 - 2.3)k_B T$ determined for optimal cuprate superconductors [46-48]. While conventional theory of strong electron-phonon scattering might mimic linearity for T between T_C and 300 K, if designed with judicious choices of residual and saturation resistivities, it appears rather implausible in view of the preponderance of $S \approx 1$ listed in Table 3 and displayed in Fig. 7.

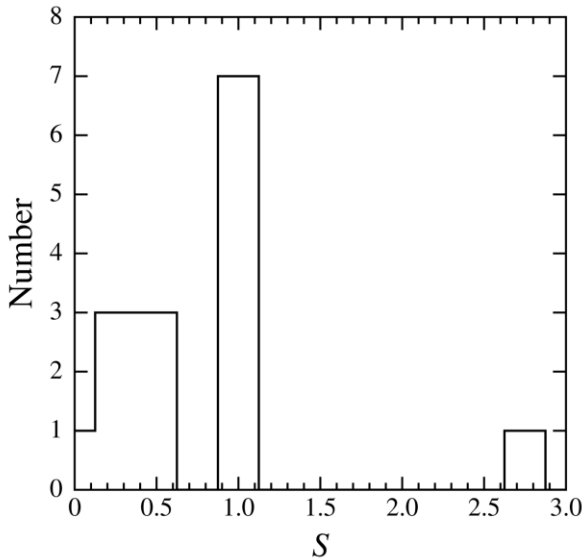


Fig. 7 Statistical distribution of data for normalized normal-state resistance temperature slope parameter S from Table 3

A3 Pressure Dependence of the Lattice Parameter

X-ray diffraction is employed to determine volumes of LaH_{10} referenced to the fcc cubic cell for samples 2 and 3 in [12] and referenced per La for superconducting samples A–C and E–G in [13]. Samples 2 and 3 are reported to contain minority phase material [12]. Samples F and G are described as mixed phase [13]. Pressure dependence in the fcc lattice parameter a are plotted in Fig. 8 as filled circles (data from [12]) and filled squares ([13]). Square symbols inscribed with a white cross correspond to samples C and E for which no information on transition temperature is provided in [13]. The straight line is a linear fit (exclusive of the two white-crossed squares) to the relation $a = a_0 - sP$

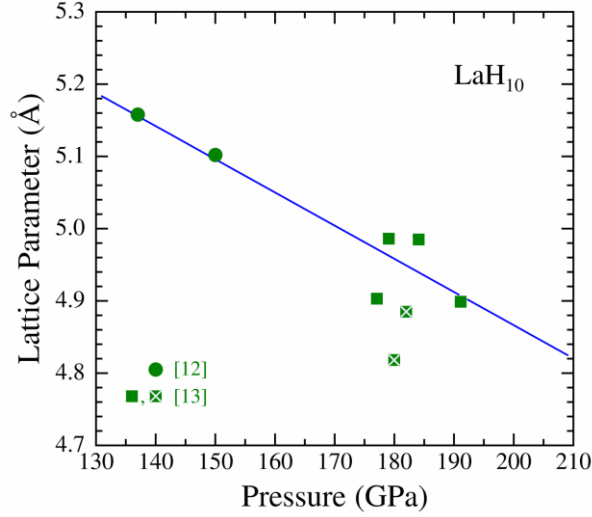


Fig. 8 Lattice parameter (face centered cubic) vs. pressure for $Fm\bar{3}m$ LaH_{10} from X-ray data in [12] (circles) and [13] (squares). The solid line shows the linear dependence obtained by fitting the data exclusive of the two white-crossed squares (see text)

with intercept $a_0 = 5.78 \pm 0.15 \text{ \AA}$, slope $s = 0.00459 \pm 0.000091 \text{ \AA/GPa}$, and root-mean-square deviation of 0.043 \AA between the data and the line. The fitted function is used to extract values of a , and therefrom d , A , ζ , ℓ , and T_{C0} , at experimental optimal pressures (Table 1).

A4 Accuracy and Systematic Error of the Model

The accuracy of Eq. (1) rests on that of the constant Λ , which was originally obtained by fitting Λ in the right-hand side expression to experimental data for T_{C0} taken for the left-hand side. The fitted data included 31 phase-pure, optimal high- T_C compounds, with superconducting transitions in the range $10.5 \text{ K} \leq T_C \leq 145 \text{ K}$ [40]. Subsequently, 24 other compounds (see [41, 49-55]), optimized according to the developed criteria and inclusive of the two LaH_{10} samples, have been added to the list of optimal superconductors with T_C values demonstrated to be in

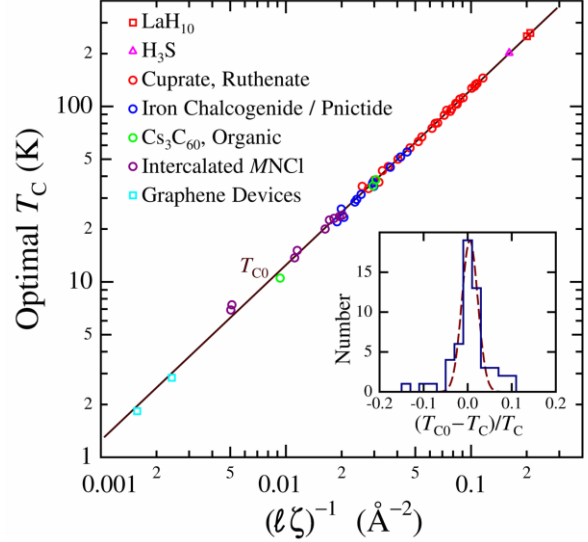


Fig. 9 Optimal measured transition temperatures T_C vs. $(\ell\zeta)^{-1}$ for 55 superconductors (grouped as per legend) are shown in comparison with calculated T_{C0} (solid line). Inset: statistical distribution of fractional deviation between calculated T_{C0} and measured T_C ; dashed curve shows fitted Gaussian form

congruence with Eq. (1), bringing the total number to 55 from eleven disparate superconducting families (with T_C ranging from ~ 2 to 260 K). Comparisons of T_{C0} calculated for LaH_{10} at 169(4) GPa [12] and at 192(4) GPa [13] with the measured average T_C values (from Table 1) yield differential accuracies of 0.48% and 0.50%, respectively. The optimal transition temperatures are predicted with an overall statistical accuracy of $\pm 4.3\%$ over a range in T_C from ~ 2 to 260 K, with an average fractional deviation of 0.7%. These results are graphically represented in Fig. 9, which plots the measured optimal transition temperature T_C vs. $(\ell\zeta)^{-1}$, and compared to the theoretical expression for T_{C0} given in Eq. (1) represented by the solid line. Deviations of T_C from the theoretical line have a root-mean-square average of 1.3 K. The statistical distribution of fractional deviation between calculated T_{C0} and measured T_C is given in the inset of Fig. 9,

where the dashed curve shows the fitted Gaussian form.

Nearly abrupt superconducting transitions are also predicted theoretically for the hydrides LaH_{10} and H_3S , by virtue of their being three-dimensional bulk crystals. One might assume that improved synthesis of the hydride samples would lead to sharper transitions, reduced uncertainty in determining T_C and, in turn, the value of Λ .

References

1. Wang, H., Tse, J. S., Tanaka, K., Iitaka, T., Ma, Y.: Superconductive sodalite-like clathrate calcium hydride at high pressures. *Proc. Nat. Acad. Sci.* **109**, 6463 (2012) Supplemental material
2. Bi, T., Zarifi, N., Terpstra, T., Zurek, E.: The search for superconductivity in high pressure hydrides. in *Elsevier Reference Module in Chemistry, Molecular Sciences and Chemical Engineering*. Reedijk, J. (ed), Elsevier (2019), pp. 1-36. <https://doi.org/10.1016/B978-0-12-409547-2.11435-0>
3. Zurek, E., Bi, T.: High-temperature superconductivity in alkaline and rare earth polyhydrides at high pressure: a theoretical perspective. *J. Chem. Phys.* **150**, 050901 (2019)
4. Flores-Livas, J. A., Boeri, L., Sanna, A., Profeta, G., Arita, R., Eremets, M.: A perspective on conventional high-temperature superconductors at high pressure: methods and materials. *Phys. Rep.* **856**, 1 (2020)
5. Liu, H., Naumov, I. I., Hoffmann, R., Ashcroft, N. W., Hemley, R. J.: Potential high- T_C superconducting lanthanum and yttrium hydrides at high pressure. *Proc. Nat. Acad. Sci.* **114**, 6990 (2017)
6. Peng, F., Sun, Y., Pickard, C. J., Needs, R. J., Wu, Q., Ma, Y.: Hydrogen clathrate structures in rare earth hydrides at high pressure: possible Route to Room-Temperature Superconductivity. *Phys. Rev. Lett.* **119**, 107001 (2017) Supplemental material
7. Li, Y., Hao, J., Liu, H., Tse, J. S., Wang, Y., Ma, Y.: Pressure-stabilized superconductive yttrium hydrides. *Sci. Rep.* **5**, 09948 (2015)
8. Heil, C., di Cataldo, S., Bachelet, G. B., Boeri, L.: Superconductivity in sodalite-like yttrium hydride clathrates. *Phys. Rev. B.* **99**, 220502(R) (2019)
9. Grishakov, K. S., Degtyarenko, N. N., Mazur E. A.: Electron, phonon, and superconducting properties of yttrium and sulfur hydrides under high pressures. *J. Exp. Theor. Phys.* **128**, 105 (2019)
10. Kvashnin, A. G., Semenov, D. V., Kruglov, I. A., Wrona, I. A., Oganov, A. R.: High-temperature superconductivity in a Th-H system under pressure conditions. *ACS Appl. Mater. Interfaces.* **10**, 43809 (2018)
11. Geballe, Z. M., Liu, H., Mishra, A. K., Ahart, M., Somayazulu, M., Meng, Y., Baldini, M., Hemley, R. J.: Synthesis and stability of lanthanum superhydrides. *Angew. Chem. Int. Ed.* **57**, 688 (2018)
12. Drozdov, A. P., Kong, P. P., Minkov, V. S., Besedin, S. P., Kuzovnikov, M. A., Mozaffari, S., Balicas, L., Balakirev, F. F., Graf, D. E., Prakapenka, V. B., Greenberg, E., Knyazev, D. A., Tkacz, M., Eremets, M. I.: Superconductivity at 250 K in lanthanum hydride under high pressures. *Nature.* **569**, 528 (2019) Supplemental material
13. Somayazulu, M., Ahart, M., Mishra, A. K., Geballe, Z. M., Baldini, M., Meng, Y., Struzhkin, V. V., Hemley, R. J.: Evidence of superconductivity above 260 K in lanthanum superhydride at megabar pressures. *Phys. Rev. Lett.* **122**, 027001 (2019) Supplemental material
14. Kong, P. P., Minkov, V. S., Kuzovnikov, M. A., Besedin, S. P., Drozdov, A. P., Mozaffari, S., Balicas, L., Balakirev, F. F., Prakapenka, V. B., Greenberg, E., Knyazev, D. A., Eremets, M. I.: Superconductivity up to 243 K in yttrium hydrides under high pressure. arXiv:1909.10482v1 [cond-mat.supr-con] (2019)
15. Troyan, I. A., Semenov, D. V., Kvashnin, A. G., Ivanova, A. G., Prakapenka, V. B., Greenberg, E., Gavriluk, A. G., Lyubutin, I. S., Struzhkin, V. V., Oganov, A. R.: Synthesis and superconductivity of yttrium hexahydride $Im\bar{3}m$ YH_6 . arXiv:1908.01534v1 [cond-mat.supr-con] (2019)
16. Semenov, D. V., Kvashnin, A. G., Ivanova, A. G., Svitlyk, V., Fominski, V. Y., Sadakov, A. V., Sobolevskiy, O. A., Pudalov, V. M., Troyan, I. A., Oganov, A. R.: Superconductivity at 161 K in thorium hydride ThH_{10} : synthesis and properties. *Materials Today.* **33**, 36 (2020) Supplemental material
17. Éliashberg, G. M.: Interactions between electrons and lattice vibrations in a superconductor. *Zh.*

- Eksp. Teor. Fiz. **38**, 966 (1960) [Sov. Phys. JETP. **11**, 696 (1960)]
18. Migdal, A. B.: Interaction between electrons and lattice vibrations in a normal metal. Zh. Eksp. Teor. Fiz. **34**, 1438 (1958) [Sov. Phys. JETP. **7**, 996 (1958)]
 19. Allen, P. B., Dynes, R. C.: Transition temperature of strong-coupled superconductors reanalyzed. Phys. Rev. B. **12**, 905 (1975)
 20. Duan, D., Yu, H., Xie, H., Cui, T.: Ab initio approach and its impact on superconductivity. J. Supercond. Nov. Magn. **32**, 53 (2019)
 21. Semenok, D. V., Kruglov, I. A., Savkin, I. A., Kvashnin, A. G., Oganov, A. R.: On distribution of superconductivity in metal hydrides. Curr. Opinion Sol. State & Mater. Sci. **24**, 100808 (2020)
 22. Liu, L., Wang, C., Yi, S., Kim, K. W., Kim, J., Cho, J.-H.: Microscopic mechanism of room-temperature superconductivity in compressed LaH₁₀. Phys. Rev. B. **99**, 140501(R) (2019)
 23. Kruglov, I. A., Semenok, D. V., Song, H., Szcześniak, R., Wrona, I. A., Akashi, R., Esfahani, M. M. D., Duan, D., Cui, T., Kvashnin, A. G., Oganov, A. R.: Superconductivity in LaH₁₀ and LaH₁₆. Phys. Rev. B. **101**, 024508 (2020) Supplemental material
 24. Wang, C., Yi, S., Cho, J.-H.: Pressure dependence of the superconducting transition temperature of compressed LaH₁₀. Phys. Rev. B. **100**, 060502(R) (2019)
 25. Errea, I., Belli, F., Monacelli, L., Sanna, A., Koretsune, T., Tadano, T., Bianco, R., Calandra, M., Arita, R., Mauri, F., Flores-Livas, J. A.: Quantum crystal structure in the 250 K superconducting lanthanum hydride. Nature. **578**, 66 (2020)
 26. Quan, Y., Ghosh, S. S., Pickett, W. E.: Compressed hydrides as metallic hydrogen superconductors. Phys. Rev. B. **100**, 184505 (2019) Supplemental material
 27. Takabayashi, Y., Ganin, A. Y., Jeglič, P., Arčon, D., Takano, T., Iwasa, Y., Ohishi, Y., Takata, M., Takeshita, N., Prassides, K., Rosseinsky, M. J.: The disorder-free non-BCS superconductor Cs₃C₆₀ emerges from an antiferromagnetic insulator parent state. Science. **323**, 1585 (2009)
 28. Hemley, R. J., Ahart, M., Liu, H., Somayazulu, M.: Road to room-temperature superconductivity: T_C above 260 K in lanthanum superhydride under pressure. arXiv:1906.03462v1 [cond-mat.supr-con] (2019)
 29. Struzhkin, V., Li, B., Ji, C., Chen, X.-J., Prakapenka, V., Greenberg, E., Troyan, I., Gavriliuk, A., Mao, H.-k.: Superconductivity in La and Y hydrides: remaining questions to experiment and theory. Matter Radiat. Extremes. **5**, 028201 (2020)
 30. Sun, D., Minkov, V. S., Kong, P., Drozdov, A., Mozaffari, S., Balicas, L., Eremets, M., Balakirev, F.: High field phase diagram of LaH₁₀. Abstract M40.0004, APS March Meeting (2020)
 31. Harshman, D. R., Mills, A. P., Jr., Concerning the nature of high- T_C superconductivity: Survey of experimental properties and implication for interlayer pairing. Phys. Rev. B. **45**, 10684 (1992)
 32. Pépin, C. M., Geneste, G., Dewaele, A., Mezouar, M., Loubeyre, P.: Synthesis of FeH₅: A layered structure with atomic hydrogen slabs. Science. **357**, 382 (2017)
 33. Majumdar, A., Tse, J. S., Wu, M., Yao, Y.: Superconductivity in FeH₅. Phys. Rev. B. **96**, 201107 (R) (2017)
 34. Kvashnin, A. G., Kruglov, I. A., Semenok, D. V., Oganov, A. R.: Iron superhydrides FeH₅ and FeH₆: stability, electronic properties and superconductivity. J. Phys. Chem. C. **122**, 4731 (2018)
 35. Heil, C., Bachelet, G. B., Boeri, L.: Absence of superconductivity in iron polyhydrides at high pressures. Phys. Rev. B. **97**, 214510 (2018)
 36. Zurek, E.: Pushing towards room-temperature superconductivity. Physics **12**, 1 (2019)
 37. Kagan, M. Y., Bianconi, A.: Fermi-Bose mixtures and BCS-BEC crossover in high- T_C superconductors. Condens. Matter. **4**, 51 (2019)
 38. Otto, H. H.: Super-hydrides of lanthanum and yttrium: on optimal conditions for achieving near room temperature superconductivity. World J. Condens. Matter Phys. **9**, 22 (2019)
 39. Talantsev, E. F.: Classifying hydrogen-rich superconductors. Mater. Res. Express. **6**, 106002 (2019)
 40. Harshman, D. R., Fiory, A. T., Dow, J. D.: Theory of high- T_C superconductivity: transition temperature. J. Phys. Condens. Matter. **23**, 295701 (2011) Corrigendum: J. Phys. Condens. Matter. **23**, 349501 (2011)
 41. Harshman, D. R., Fiory, A. T.: Compressed H₃S: inter-sublattice Coulomb coupling in a high- T_C superconductor. J. Phys. Condens. Matter. **29**, 445702 (2017)

42. Harshman, D. R., Fiory, A. T.: On the isotope effect in compressed H_3S and D_3S . *Supercond. Sci. Technol.* **30**, 045011 (2017)
43. Gurvitch, M., Fiory, A. T.: Resistivity of $\text{La}_{1.825}\text{Sr}_{0.175}\text{CuO}_4$ and $\text{YBa}_2\text{Cu}_3\text{O}_7$ to 1100 K: absence of saturation and its implications. *Phys. Rev. Lett.* **59**, 1337 (1987)
44. Legros, A., Benhabib, S., Tabis, W., Laliberté, F., Dion, M., Lizaire, M., Vignolle, B., Vignolles, D., Raffy, H., Li, Z. Z., Auban-Senzier, P., Doiron-Leyraud, N., Fournier, P., Colson, D., Taillefer, L., Proust, C.: Universal T -linear resistivity and Planckian dissipation in overdoped cuprates. *Nature Phys.* **15**, 142 (2019)
45. Zaanen, J.: Planckian dissipation, minimal viscosity and the transport in cuprate strange metals. *SciPost Phys.* **6**, 061 (2019)
46. Kamarás, K., Herr, S. L., Porter, C. D., Tache, N., Tanner, D. B., Etemad, S., Venkatesan, T., Chase, E., Inam, A., Wu, X. D., Hegde, M. S., Dutta, B.: In a clean high- T_C superconductor you do not see the gap. *Phys. Rev. Lett.* **64**, 84 (1990) Erratum: *Phys. Rev. Lett.* **64**, 1692 (1990)
47. Fiory, A. T., Hebard, A. F., Eick, R. H., Mankiewich, P. M., Howard, R. E., O'Malley, M. L.: Metallic and superconducting surfaces of $\text{YBa}_2\text{Cu}_3\text{O}_7$ probed by electrostatic charge modulation of epitaxial films. *Phys. Rev. Lett.* **65**, 3441 (1990)
48. Romero, D. B., C. Porter, D., Tanner, D. B., Forro, L., Mandrus, D., Mihaly, L., Carr, G. L., Williams, G. P.: Quasiparticle damping in $\text{Bi}_2\text{Sr}_2\text{CaCu}_2\text{O}_8$ and $\text{Bi}_2\text{Sr}_2\text{CuO}_6$. *Phys. Rev. Lett.* **68**, 1590 (1992)
49. Harshman, D. R., Fiory, A. T.: High- T_C superconductivity in Cs_3C_{60} compounds governed by local Cs – C_{60} Coulomb interactions. *J. Phys. Condens. Matter.* **29**, 145602 (2017)
50. Harshman, D. R., Fiory, A. T.: Charge compensation and optimal stoichiometry in superconducting $(\text{Ca}_x\text{La}_{1-x})(\text{Ba}_{1.75-x}\text{La}_{0.25+x})\text{Cu}_3\text{O}_y$. *Phys. Rev. B.* **86**, 144533 (2012)
51. Harshman, D. R., Fiory, A. T.: Superconducting interaction charge in thallium-based high- T_C cuprates: roles of cation oxidation state and electronegativity. *J. Phys. Chem. Sol.* **85**, 106 (2015)
52. Harshman, D. R., Fiory, A. T.: The superconducting transition temperatures of $\text{Fe}_{1+x}\text{Se}_{1-y}$, $\text{Fe}_{1+x}\text{Se}_{1-y}\text{Te}_y$ and $(\text{K/Rb/Cs})_z\text{Fe}_{2-x}\text{Se}_2$. *J. Phys. Condens. Matter.* **24**, 135701 (2012)
53. Harshman, D. R., Fiory, A. T.: Comment on “Superconductivity in electron-doped layered TiNCl with variable interlayer coupling”. *Phys. Rev. B.* **90**, 186501 (2014)
54. Harshman, D. R., Fiory, A. T.: Modeling intercalated group-4-metal nitride halide superconductivity with interlayer Coulomb coupling. *J. Supercond. Nov. Magn.* **28**, 2967 (2015)
55. Harshman, D. R., Fiory, A. T.: High- T_C superconductivity originating from interlayer Coulomb coupling in gate-charged twisted bilayer graphene Moiré superlattices. *J. Supercond. Nov. Magn.* **33**, 367 (2020)
56. Mozaffari, S., Sun, D., Minkov, V. S., Drozdov, A. P., Knyazev, D., Betts, J. B., Einaga, M., Shimizu, K., Eremets, M. I., Balicas, L., Balakirev, F. F.: Superconducting phase diagram of H_3S under high magnetic fields. *Nature Commun.* **10**, 2522 (2019)
57. Drozdov, A. P., Eremets, M. I., Troyan, I. A., Ksenofontov, V., Shylin, S. I.: Conventional superconductivity at 203 Kelvin at high pressures in the sulfur hydride system. *Nature.* **525**, 73 (2015)
58. Oh, H., Coh, S., Cohen, M. L.: Comparative study of high- T_C superconductivity in H_3S and H_3P . arXiv:1606.09477v2 [cond-mat.supr-con] (2016)
59. Duan, D., Liu, Y., Tian, F., Li, D., Huang, X., Zhao, Z., Yu, H., Liu, B., Tian, W., Cui, T.: Pressure-induced metallization of dense $(\text{H}_2\text{S})_2\text{H}_2$ with high- T_C superconductivity. *Sci. Rep.* **4**, 6968 (2014)
60. Papaconstantopoulos, D. A., Klein, B. M., Mehl, M. J., Pickett, W. E.: Cubic H_3S around 200 GPa: an atomic hydrogen superconductor stabilized by sulfur. *Phys. Rev. B.* **91**, 184511 (2015)
61. Boeri, L. Bachelet, G. B.: Viewpoint: the road to room-temperature conventional superconductivity. *J. Phys. Condens. Matter.* **31**, 234002 (2019)
62. Salke, N. P., Esfahani, M. M. D., Zhang, Y., Kruglov, I. A., Zhou, J., Wang, Y., Greenberg, E., Prakapenka, V. B., Liu, J., Oganov, A. R., Lin, J.-F.: Synthesis of clathrate cerium superhydride CeH_9 at 80-100 GPa with atomic hydrogen sublattice. *Nat. Commun.* **10**, 4453 (2019)
63. Zhou, D., Semenok, D. V., Duan, D., Xie, H., Chen, W., Huang, X., Li, X., Liu, B., Oganov, A. R., Cui, T.: Superconducting praseodymium superhydrides. *Sci. Adv.* **5**, eaax6849 (2020)
64. Kim, D. Y., Scheicher, R. H., Ahuja, R.: Predicted high-temperature superconducting state in the

- hydrogen-dense transition-metal hydride YH_3 at 40 K and 17.7 GPa. *Phys. Rev. Lett.* **103**, 077002 (2009)
65. Jarosik, M. W., Szcześniak, R., Wrona, I. A., Kostrzewa, M.: Non-BCS superconducting state in yttrium hydride at a record low value of the external pressure. *Sol. State Commun.* **250**, 5 (2017)
 66. Ohmura, A., Machida, A., Watanuki, T., Aoki, K., Nakano, S., Takemura, K.: Infrared spectroscopic study of the band-gap closure in YH_3 at high pressure. *Phys. Rev. B.* **73**, 104105 (2006)
 67. Kume, T., Ohura, H., Sasaki, S., Shimizu, H., Ohmura, A., Machida, A., Watanuki, T., Aoki, K., Takemura, K.: High-pressure study of YH_3 by Raman and visible absorption spectroscopy. *Phys. Rev. B.* **76**, 024107 (2007)
 68. Soerensen, G., Gygax, S.: Evaluation of oxygen isotope experiments on Pr-, Ca-, and Zn-substituted $\text{YBa}_2\text{Cu}_3\text{O}_7$. *Phys. Rev. B.* **51**, 11848 (1995)
 69. Harshman, D. R., Dow, J. D., Fiory, A. T.: Isotope effect in high- T_C superconductors. *Phys. Rev. B.* **77**, 024523 (2008)
 70. Harshman, D. R., Dow, J. D., Fiory, A. T.: Reply to “Comment on ‘Isotope effect in high- T_C superconductors’”. *Phys. Rev. B.* **80**, 136502 (2009)
 71. Shao, Z., Duan, D., Ma, Y., Yu, H., Song, H., Xie, H., Li, D., Tian, F., Liu, B., Cui, T.: Unique phase diagram and superconductivity of calcium hydrides at high pressures. *Inorg. Chem.* **58**, 2558 (2019)
 72. Qian, S., Sheng, X., Yan, X., Chen, Y., Song, B.: Theoretical study of stability and superconductivity of ScH_n ($n = 4-8$) at high pressure. *Phys. Rev. B.* **96**, 094513 (2017)
 73. Semenok, D., Kvashnin, A. G., Kruglov, I. A., Oganov, A. R.: Actinium hydrides AcH_{10} , AcH_{12} and AcH_{16} as high-temperature conventional superconductors. *J. Phys. Chem. Lett.* **9**, 1920 (2018)
 74. Li, X., Huang, X., Duan, D., Pickard, C. J., Zhou, D., Xie, H., Zhuang, Q., Huang, Y., Zhou, Q., Liu, B., Cui, T.: Polyhydride CeH_9 with an atomic-like hydrogen clathrate structure. *Nat. Commun.* **10**, 3461 (2019)
 75. Pěna-Alvarez, M., Binns, J., Hermann, A., Kelsall, L. C., Dalladay-Simpson, P., Gregoryanz, E., Howie, R. T.: Praseodymium polyhydrides synthesized at high temperatures and pressures. *Phys. Rev. B.* **100**, 184109 (2019)
 76. Gor’kov, L. P., Kresin, V. Z.: Colloquium: High pressure and road to room temperature superconductivity. *Rev. Mod. Phys.* **90**, 011001 (2018)
 77. Baldassarre, L., Perucchi, A., Mitrano, M., Nicoletti, D., Marini, C., Pontiroli, D., Mazzani, M., Aramini, M., Riccò, M., Giovannetti, G., Capone, M., Lupi, S.: The strength of the electron electron correlation in Cs_3C_{60} . *Sci. Rep.* **5**, 15240 (2015)
 78. Capitani, F., Langerome, B., Brubach, J.-B., Roy, P., Drozdov, A., Eremets, M. I., Nicol, E. J., Carbotte, J. P., Timusk, T.: Spectroscopic evidence of a new energy scale for superconductivity in H_3S . *Nat. Phys.* **13**, 859 (2017)
 79. Carbotte, J. P., Nicol, E. J., Timusk, T.: Spectroscopic signatures of phonons in high pressure superconducting hydrides. *Phys. Rev. B.* **100**, 094505 (2019).
 80. Bill, A., Morawitz, H., Kresin, V. Z.: Electronic collective modes and superconductivity in layered conductors. *Phys. Rev. B.* **68**, 144519 (2003)
 81. Shipley, A. M., Hutcheon, M. J., Johnson, M. S., Needs, R. J., Pickard, C. J.: Stability and superconductivity of lanthanum and yttrium decahydrides. [arXiv:2001.05305v2](https://arxiv.org/abs/2001.05305v2) [cond-mat.supr-con] (2020)